Length of main text: 2956 words
Length of methods: 3605 words
Length of legends: 565 words
Number of references: 53 main text, 69 including methods and supplementary information
(refs 67 to 69 are cited in the SI only)
Number of figures: 6 main, 8 supplementary. Main figures submitted as AI/PDF and PDS/JPEG.
Fig. 2 would be best at two columns.

The Regolith of (101955) Bennu from OSIRIS-REx Imaging and Thermal Analysis

Authors and affiliations

D. N. DellaGiustina[1†], J. P. Emery[2†], D. R. Golish[1], B. Rozitis[3], C. A. Bennett[1], K. N. Burke[1], R.-L. Ballouz[1], K. J. Becker[1], P. R. Christensen[4], C. Y. Drouet d'Aubigny[1], V. E. Hamilton[5], D. C. Reuter[6], B. R. Rizk[1], A. A. Simon[6], E. Asphaug[1], J. L. Bandfield[7], O. S. Barnouin[8], M. A. Barucci[9], E. B. Bierhaus[10], R. P. B. Binzel[11], W. F. Bottke[5], N. Bowles[12], H. Campins[13], B. C. Clark[7], B. E. Clark[14], H. C. Connolly Jr.[15], M. Daly[16], J. de Leon[17,18], M. Delbó[19], J. D. P. Deshapriya[9], C. M. Elder[20], S. Fornasier[9], C. W. Hergenrother[1], E. S. Howell[1], E. R. Jawin[21], H. H. Kaplan[5], T. Kareta[1], L. Le Corre[22], J.-Y. Li[22], J. Licandro[17,18], L. F. Lim[6], P. Michel[19], J. Molaro[20], M. Nolan[1], M. Pajola[23], M. Popescu[17,18], J. L. Rizos Garcia[17,18], A. Ryan[19], S. R. Schwartz[1], N. Shultz[1], M. A. Siegler[24], P. H. Smith[1], E. Tatsumi[25], C. A. Thomas[26], K. J. Walsh[5], C. W. V. Wolner[1], X.-D. Zou[22], D. S. Lauretta[1], and the OSIRIS-REx Team.

[1]Lunar and Planetary Laboratory, University of Arizona, Tucson, AZ 85705, USA.
[2]Department of Earth and Planetary Sciences, University of Tennessee, Knoxville, TN 37996, USA.
[3]School of Physical Sciences, Open University, Milton Keynes MK7 6AA, UK.
[4]Department of Geological Science, Arizona State University, Tempe, AZ 85281, USA.
[5]Southwest Research Institute, Boulder, CO 80302, USA.
[6]NASA Goddard Space Flight Center, Greenbelt, MD 20771, USA.
[7]Space Science Institute, Boulder, CO 80301, USA.
[8]The Johns Hopkins University Applied Physics Laboratory, Laurel, MD 20723, USA.
[9]LESIA-Observatoire de Paris, CNRS, PSL, Sorbonne Université, Université Paris-Diderot, 92195 Meudon Principal Cedex, France.
[10]Lockheed-Martin Space Systems Company, Littleton, CO 80201, USA.
[11]Earth, Atmospheric and Planetary Sciences Department, Massachusetts Institute of Technology, Cambridge, MA 02139, USA.
[12]Atmospheric Physics, University of Oxford, Oxford OX1 2JD, UK.
[13]Department of Physics, University of Central Florida, Orlando, FL 32816, USA.
[14]Department of Physics and Astronomy, Ithaca College, Ithaca, NY 14850, USA.
[15]Department of Geology, School of Earth & Environment, Rowan University, Glassboro, NJ 08028, USA.
[16]Centre for Research in Earth and Space Science, York University, Toronto, ON, Canada M3J 1P3.
[17]Instituto de Astrofísica de Canarias, C/Vía Láctea s/n, E-38205 La Laguna, Tenerife, Spain.
[18]Departamento de Astrofísica, Universidad de La Laguna, E-38206 La Laguna, Tenerife, Spain.
[19]Université Côte d'Azur, Observatoire de la Côte d'Azur, CNRS, France.
[20]Jet Propulsion Laboratory, Pasadena, CA 91109, USA.

[21]Department of Mineral Sciences, National Museum of Natural History, Smithsonian Institution, Washington, DC 20013, USA.

[22]Planetary Science Institute, Tucson, AZ 85719, USA.

[23]Istituto Nazionale di Astrofisica, Astronomical Observatory of Padova, 35122 Padova PD, Italy.

[24]Department of Earth Sciences, Southern Methodist University, Dallas, TX 75275, USA.

[25]Department of Earth and Planetary Science, The University of Tokyo, Bunkyō, Tokyo 113-8654, Japan.

[26]Department of Physics and Astronomy, Northern Arizona University, Flagstaff, AZ 86001, USA.

[†] These authors contributed equally to this work.

Establishing the abundance and physical properties of regolith and boulders on asteroids is crucial for understanding the formation and degradation mechanisms at work on their surfaces. Using images and thermal data from NASA's Origins, Spectral Interpretation, Resource Identification, and Security–Regolith Explorer (OSIRIS-REx) spacecraft, we show that asteroid (101955) Bennu's surface is globally rough, dense with boulders and low in albedo. The number of boulders is surprising given Bennu's moderate thermal inertia, suggesting that simple models linking thermal inertia to particle size do not adequately capture the complexity relating these properties. At the same time, we find evidence for a wide range of particle sizes with distinct albedo characteristics. Our findings imply that ages of Bennu's surface particles span from the disruption of the asteroid's parent body (boulders) to recent in situ production (micron-scale particles).

Before the OSIRIS-REx mission, expectations for the distribution of regolith on small near-Earth asteroids (NEAs) came from (25143) Itokawa and (162173) Ryugu, where smooth terrains are evident at global scales. Likewise, our understanding of Bennu's global properties was inferred from telescopic observations of the asteroid as a point source [1]. In late 2018, the OSIRIS-REx spacecraft rendezvoused with asteroid (101955) Bennu and acquired remotely sensed image and spectral data. The OSIRIS-REx Camera Suite (OCAMS [2]) PolyCam panchromatic camera confirmed the top-like shape of the asteroid [3] and imaged the surface at scales down to 0.33 m/pixel, while the MapCam instrument imaged at scales down to 1.1 m/pixel in four colors and a panchromatic filter. The OSIRIS-REx Visible and InfraRed Spectrometer (OVIRS [4]) and the OSIRIS-REx Thermal Emission Spectrometer (OTES [5]) measured disk-integrated spectra covering a full asteroid rotation before Bennu filled their respective fields of view.

Global Average Properties

During the Approach and Preliminary Survey phases of the mission (August to December 2018), we measured Bennu's resolved reflectance (I/F) in MapCam's five filters across a wide range of phase angles (0.7° to 90°). Fitting these data to an exponential phase function [6] yields a low global average geometric albedo of 4.4% ± 0.2% at 550 nm (Fig. 1a). This albedo is consistent with ground-based astronomical data [7], B-type asteroid taxonomy [8], and results from OSIRIS-REx disk-integrated photometry [9]. The global albedo is also compatible with the

reflectance of CM chondrite meteorites [10], which are spectroscopically similar to Bennu [11]. Bennu does not exhibit a significant opposition surge at low phase angles. The absence of a strong opposition effect is not surprising given the low albedo and thus single-scattering nature of the surface [6].

During Approach, we also acquired disk-integrated and rotationally resolved measurements of Bennu's thermal radiance from OVIRS and OTES. From these data, we determine a global average thermal inertia of 350 ± 20 J m^{-2} K^{-2} s$^{-1/2}$ (Supplementary Figs. 1 and 2, methods, supplementary information). The OSIRIS-REx thermal data constrain thermal inertia variations to < 10 J m^{-2} K^{-1} s$^{-1/2}$ over a full rotation. The low to moderate thermal inertia and small variability with rotation are within the uncertainties of previous results based on observations with the Spitzer Space Telescope [12].

The thermal inertia of asteroid surfaces is often translated into a characteristic particle size using simplified models that assume a uniform particulate regolith [e.g., 12-14]. The basis for these models is that particles smaller than the diurnal thermal skin depth will produce a thermal inertia smaller than the value for bedrock (1500 to 2500 J m^{-2} K^{-1} s$^{-1/2}$ for typical planetary materials [15,16]). For the moderate thermal inertia measured for Bennu, these models predict a surface dominated by 0.5- to 5-cm-diameter particles (methods, supplementary information). However, resolved images of Bennu's surface show that it is in fact dominated by >1-m boulders (Fig. 2).

The simplistic regolith models clearly do not accurately describe Bennu's surface. Below, we discuss other possible interpretations of Bennu's thermal inertia, including low thermal inertia of boulders, dust cover on boulders, a mixture of particulate regolith and boulders, or a combination of these effects.

Spatially Resolved Surface Morphology and Boulder Distribution

Bennu is geomorphologically diverse (Fig. 2), cratered, and covered by rocks with a wide range of sizes, consistent with its characterization as a rubble-pile asteroid [17]. Impact craters range in size from 10 to over 150 m [18], and the surface is populated by more than 200 boulders >10 m in diameter. The largest boulders exceed 30 m and appear predominantly at high latitudes. Smaller meter-scale boulders are evenly distributed across the asteroid, consistent with the uniform thermal inertia with rotation. Boulders display a wide range of morphology, sizes, and albedo. One of the darkest objects is the partially exposed outcrop of a boulder in the southern (–Z) hemisphere (–20° latitude, 30° longitude), perhaps a constituent component of the asteroid. It measures nearly 100 m in observable longest dimension, but its full extent is unclear. Bennu exhibits only small areas (<20 m) of boulder-free regolith [19], contrary to pre-encounter expectations [1,12,20].

We have completed boulder counts and size measurements for > 80% of the asteroid's surface (Supplementary Fig. 3). The measured sizes of the boulders range from 1 to 58 m (longest dimension). Figure 3 depicts the global cumulative size-frequency distribution (CSFD) of Bennu,

with a power-law index of –2.9 ± 0.3 for boulders 8 m and larger (see methods for a discussion of the statistical completeness limit). This power-law index is within the range of other small Solar System bodies (Supplementary Fig. 4).

By comparison, asteroid (25143) Itokawa has a global power-law index of –3.5 ± 0.1[21] for boulders ≥ 10 m, which implies that more of its surface mass is contained in small particles than is the case for Bennu. This is consistent with the distinct appearance of these two asteroids—Bennu lacks Itokawa's smooth regions such as the Muses Sea [22]. However, the absolute number density of large boulders (≥20 m) on Bennu and Itokawa is comparable (28.2 km^{-2} vs. ~25 km^{-2}) [21,22]. Conversely, the number density of boulders ≥20 m on Bennu is about half that on asteroid (162173) Ryugu (~50 km^{-2}), the slightly larger top-shaped target of the Hayabusa2 mission. Like Bennu, Ryugu has a power-law index of –2.5 to –3.0. This suggests that while the absolute number of large boulders on rubble-pile NEAs is scaled by asteroid size, surface particle distributions may be distinct on top-shaped objects. Notably, the distribution of the large boulders (≥20 m) at high latitudes on Bennu corresponds with a steepening in the dynamic surface slope outside of the equatorial latitudes [23]. Accordingly, material from mid-latitude to polar regions is less energetically coupled to the surface of the asteroid [23]. As a result, smaller particles may preferentially migrate away from these areas, resulting in the exhumation and retention of larger boulders at higher latitudes.

A shallow power-law index suggests boulder production dominated by impact processes [24]. While multiple candidate impact craters [18] are visible across the surface (Fig. 2), the events that formed them could not produce the large observed boulder population (Supplementary Fig. 5). The presence of intact blocks about 1/10th of the diameter of Bennu suggests that the largest boulders are fragments from the catastrophic disruption of its parent body and the subsequent rubble-pile reaccumulation [18,25]. Thus, the large (≥ 20 m) boulders evident in Bennu's relatively shallow CSFD represent some of the oldest intact material on the surface. Although boulders <20 m may have been inherited by the catastrophic disruption of Bennu's parent body, it is likely that some were formed by impacts on Bennu's own surface, and may have experienced further in-situ breakdown and disaggregation by thermal fatigue [26].

Physical Properties of Boulders

Bennu's thermal inertia may be conveying information about the physical properties of its large surface boulders. One interpretation of the moderate thermal inertia is that the large boulders could have a lower thermal inertia than typical planetary materials. Any property that impedes the thermal wave in the material could lower the thermal inertia (e.g., porosity, cement between clasts of a breccia, amorphous material). For example, the CM chondrite Cold Bokkeveld has a low thermal conductivity and correspondingly low thermal inertia (~770 J m^{-2} K^{-1} $s^{-1/2}$ [16]) due its porosity (~15%) [27]. The hypothesis that Bennu's boulders themselves have a relatively low thermal inertia is supported by the close spectral match of Bennu's surface to CM chondrites [11]. However, the thermal inertia of Cold Bokkeveld (the lowest among measured meteorites [27]) is still considerably larger than Bennu's global value. We investigated the thermal inertia of the boulders on Bennu by running a two-component thermal

model constrained by the spatial density of boulders presented in a companion paper [18]. We find that the upper limit on the average boulder thermal inertia on Bennu is 1400 J m^{-2} K^{-1} s$^{-1/2}$. We will measure thermal inertia of individual boulders from upcoming spatially resolved thermal observations.

The global thermal inertia of Itokawa (750 J m^{-2} K^{-1} s$^{-1/2}$) [28] is more than twice Bennu's, even though the number density of large boulders is comparable. The shallower CSFD power-law index on Bennu suggests that it may have fewer centimeter-scale particles than Itokawa. Although it is not yet known whether Bennu's CSFD maintains a constant power-law index from 8 m to 2 cm, analyses of regolith on other asteroids suggest constant power laws across similar scales (e.g., [29]). The lower thermal inertia and relative deficit of small particles on Bennu, in turn, suggest that the boulders may have a lower thermal inertia than those on Itokawa. Different thermal inertias of boulders on S-type versus B-type asteroids are consistent with differences in the thermal conductivity of their respective analog meteorites [27]. Density and heat capacity also influence thermal inertia, but their variation among meteorite analogs is much smaller than that of thermal conductivity. Although the boulder abundance on Ryugu is about twice that on Bennu and the CSFD indices are similar, Ryugu's thermal inertia is 200 to 500 J m^{-2} K^{-1} s$^{-1/2}$ [30,31], suggesting that its boulders may have similar thermal inertia to Bennu's. Porosity tends to have a stronger control on thermal inertia than composition [27], so the difference in Itokawa's global thermal inertia compared to Bennu's and Ryugu's could result from distinct porosities of their boulders.

Boulders are a major source of albedo heterogeneity on Bennu. The full range of normal albedo variation is more than a factor of 4 (from 3.3% to 15%), though 95% of the range is between 3.6% to 4.8% (a factor of 1.5 [19]). This diversity is greater than on Ryugu, which has a similar global geometric albedo to Bennu [31]. The total range also exceeds that observed on Itokawa (factor of 1.3 [32]) and Eros (factor of 3.5 [33]). Because much of Bennu's albedo variation appears linked to boulder size, trends in albedo may help us assess the properties of these boulders. Fig. 4a shows the normal albedo distribution of boulders identified to date. The largest boulders have albedos near the global average, whereas the brightest boulders (>1σ from the mean boulder albedo, or >6.8%) are all smaller than ~10 m. Although we are only sampling a small number of bright boulders (~370), our data show a clear difference in the size distributions of bright versus average-to-dark boulders (Fig. 4b).

This distinct size distribution has several potential origins. Much of the spectrophotometric variation observed on airless bodies has been attributed to radiation and bombardment processes collectively referred to as "space weathering". For example, on asteroid (433) Eros, color and reflectance differences are not explained by distinct rock types, but rather by complex regolith sorting and space weathering processes [34]. Lantz et al. [35] investigated solar wind–induced space weathering outcomes for CI/CM chondrites and predicted that bluer and brighter regions on Bennu could represent more weathered material, although results from laser irradiation experiments show the opposite [36]. Given that the large (> 30 m) boulders represent intact material from Bennu's parent body, their average albedo may signify older

surfaces that have been more optically modified. Smaller and brighter boulders may represent younger, more recently fragmented material.

Another possibility is that bright material represents remnants of Bennu's parent body or the impactor that disrupted it, which reaccreted into Bennu and other small asteroids. This scenario would imply that the observed heterogeneity is the result of distinct rock types, which fragment differently, leading to the observed differences in size distribution. Some clues are provided from evidence of bright clasts bound in a matrix [19] and in situ boulder disaggregation into resistant constituent clasts (Fig. 5). Lauretta et al. [19] show that some clasts have a range of albedos that differ from the surrounding terrain, implying that some of the albedo diversity on Bennu is inherited.

Evidence of Particulate Regolith

We observe diffuse units of dark material that we interpret as low-albedo dust blanketing the surface (Fig. 6, Supplementary Fig. 6). The dark diffuse unit shown in Fig. 6 is proximal to the partially exposed boulder outcrop (discussed above), which is one of the darkest objects on the asteroid and shows a spectral feature at 550 nm [19]. Lauretta et al. [19] suggest that this spectral feature is due to enhanced magnetite concentrations generated as a byproduct of space weathering. Our observation of dark dust cover strengthens this finding by supplying evidence that it is compositionally distinct. Laboratory studies show that the reflectance of CM chondrite powders increases with decreasing particle size [37]. Thus, dust generated from mechanical breakdown on Bennu should be brighter, and for dust to be darker than the surroundings, it likely has a different composition. However, the mechanism for transporting fine material from a compositionally distinct reservoir to nearby terrains remains unclear.

Furthermore, the presence of particulate regolith mixed with the observed boulders could explain the moderate thermal inertia. If such fine-particulate material manifested as a dust (particle size < few 10s of microns) coating on boulders, as we observe, it would result in a masking of the higher-thermal-inertia signature expected from large boulders. Dust coatings a few 10s to 100 μm thick affect thermal signatures [38]. Particulates may also be present as coarser regolith between boulders, or as a combination of dust coating and coarser interstitial regolith. Indeed, images of the surface reveal some areas that appear smooth at current pixel scales (33 cm/pixel) [19], indicating the presence of particulate regolith.

The global scattering properties of Bennu obtained from spectrophotometric modeling reveal additional evidence of small particles. The spectral dependence of Bennu's phase curve is nearly flat to within the radiometric precision of OCAMS (Fig 1a). In relative comparisons between the OCAMS colors, however, Bennu reddens at higher phase angles (Fig. 1b), as has been observed on several other asteroids [39,40]. Bennu's low albedo does not favor multiple scattering, which has been invoked to explain phase reddening [41]. Although single scattering is typically considered to have a weak wavelength dependence, Li et al. [40] suggest that wavelength-dependent single scattering on low-albedo surfaces might be due to micron-scale particles. This inference is supported by laboratory analyses demonstrating that the external

structure of small scatterers can exhibit wavelength-dependent interactions with light [42]. As the wavelength begins to exceed the size of the scatterer, small grains become less opaque, leading to a relative increase in reflectance. The observed phase reddening thus implies the presence of micron-scale material on the surface. The presence of fine particles is consistent with one possible interpretation of the moderate global thermal inertia: a dust coating on boulders. Reflectance and thermal emission spectra are also consistent with the presence of fine particulates among the abundant boulders [11].

Finally, our thermal analysis finds that Bennu has a rough surface (RMS slope of 43 ± 1°, Supplementary Fig. 2). This roughness is comparable to that of other asteroids [43–46] but rougher than that of the Moon [47]. The model itself does not set a spatial scale for this roughness; it can be anywhere between the resolution of the shape model used for the thermal analysis (~12 m) and the diurnal thermal skin depth (~2 cm, methods), though we expect that roughness at the smaller length scales dominates the thermal signature [43]. From the shape model of Bennu [3], we find RMS slopes that increase with decreasing spatial scale. Extrapolation of a power-law fit to roughness estimates from the shape model at four spatial scales fits the measured thermal roughness at a spatial scale of ~2 cm (Supplementary Fig. 7). We therefore predict that the surface of Bennu is rough at small spatial scales, perhaps consistent with the images of Ryugu returned by the MASCOT lander [48]. Images of the surface of Bennu during the Reconnaissance phase of the mission will test this prediction.

The presence of micron-scale particles on Bennu runs counter to the expectation that small (>1 km) airless bodies have coarser regolith because their lower gravity hinders retention of fines (which escape the surface through impact events, solar wind pressure, and centripetal forces [13,49,50]). However, it is consistent with the findings of the Hayabusa mission, which collected micron-size particles from the surface of Itokawa [51]. The presence of such particles implies an enhanced ability of the finest material to remain coupled to the surface through electrostatic effects [52], or the ongoing production of particles through micrometeorite impacts [51] and thermal fatigue of boulders [26] on timescales shorter than the loss mechanisms.

Conclusion and Perspectives

Our initial findings from imaging and thermal data reveal a rubble-pile asteroid with extensive surficial diversity. There exists a heterogeneity of particle sizes on the surface. Large-scale boulders imply the presence of intact materials that originated at or before the disruption of Bennu's parent body, whereas evidence of micron-scale particles point to more recent in situ production and retention of fines on the surface of the asteroid. The thermal inertia of Bennu suggests either a substantial population of centimeter-scale particles among the surface boulders, thin dust cover blanketing the boulders, high porosity of the boulders, or a combination of these. Despite the inferred range of particle sizes, there are no large areas of well-sorted particulate regolith. The presence of bright boulders with a distinct size-frequency distribution may be primordial—perhaps, exposed fragments of a heterogeneous parent body that was collisionally disrupted. Conversely, their presence could be explained as fresher material that has undergone less optical surface modification via space weathering. We will test

these hypotheses with observations at higher spatial and spectral resolutions planned for the Detailed Survey [53] phase of the mission in the spring of 2019.

References

1. Lauretta, D. S. *et al.* The OSIRIS-REx target asteroid (101955) Bennu: Constraints on its physical, geological, and dynamical nature from astronomical observations. *Meteorit. Planet. Sci.* **50**, 834–849 (2015).
2. Rizk, B. *et al.* OCAMS: The OSIRIS-REx Camera Suite. *Space Sci. Rev.* **214**, 26 (2018).
3. Barnouin, O. S. *et al*. Shape of (101955) Bennu indicative of a rubble pile with internal stiffness. *Nat. Geosci.*, in press.
4. Reuter, D. C. *et al.* The OSIRIS-REx Visible and InfraRed Spectrometer (OVIRS): Spectral Maps of the Asteroid Bennu. *Space Sci. Rev.* **214**, 54 (2018).
5. Christensen, P. R. *et al.* The OSIRIS-REx Thermal Emission Spectrometer (OTES) Instrument. *Space Sci. Rev.* **214**, 87 (2018).
6. Li, J.-Y., Helfenstein, P., Buratti, B., Takir, D. & Clark, B. E. Asteroid Photometry. in *Asteroids IV* **086**, 277–326 (University of Arizona Press, Tucson, AZ, 2015).
7. Hergenrother, C. W. *et al.* Lightcurve, Color and Phase Function Photometry of the OSIRIS-REx Target Asteroid (101955) Bennu. *Icarus* **226**, 663–670 (2013).
8. Alí-Lagoa, V. *et al.* Differences between the Pallas collisional family and similarly sized B-type asteroids. *Astron. Astrophys.* **591**, A14 (2016).
9. Hergenrother, C. W. *et al*. Operational environment and rotational acceleration of asteroid (101955) Bennu from OSIRIS-REx observations. *Nat. Commun.*, in press.
10. Clark, B. E. *et al.* Asteroid (101955) 1999 RQ36: Spectroscopy from 0.4 to 2.4μm and meteorite analogs. *Icarus* **216**, 462–475 (2011).
11. Hamilton, V. E. *et al*. Evidence for widespread hydrated minerals on asteroid (101955) Bennu. *Nat. Astron.*, in press.
12. Emery, J. P. *et al.* Thermal infrared observations and thermophysical characterization of OSIRIS-REx target asteroid (101955) Bennu. *Icarus* **234**, 17–35 (2014).
13. Gundlach, B. & Blum, J. A new method to determine the grain size of planetary regolith. *Icarus* **223**, 479–492 (2013).
14. Delbó, M., Mueller, M., Emery, J. P., Rozitis, B. & Capria, M. T. Asteroid Thermophysical Modeling. in *Asteroids IV* (University of Arizona Press, 2015).
15. Jakosky, B. M. On the thermal properties of Martian fines. *Icarus* **66**, 117–124 (1986).
16. Opeil, C. P., Consolmagno, G. J. & Britt, D. T. The thermal conductivity of meteorites: New measurements and analysis. *Icarus* **208**, 449–454 (2010).
17. Walsh, K. J. Rubble Pile Asteroids. *Annu. Rev. Astron. Astrophys.* **56**, 593–624 (2018).
18. Walsh, K. J. *et al*. Craters, boulders and regolith of (101955) Bennu indicative of an old and dynamic surface. *Nat. Geosci.*, in press.
19. Lauretta, D. S., DellaGiustina, D. N. *et al*. The unexpected surface of asteroid (101955) Bennu. *Nature*, in press.
20. Nolan, M. C. *et al.* Shape model and surface properties of the OSIRIS-REx target Asteroid (101955) Bennu from radar and lightcurve observations. *Icarus* **226**, 629–640 (2013).
21. Mazrouei, S., Daly, M. G., Barnouin, O. S., Ernst, C. M. & DeSouza, I. Block distributions on Itokawa. *Icarus* **229**, 181–189 (2014).

22.   Michikami, T. *et al.* Size-frequency statistics of boulders on global surface of asteroid 25143 Itokawa. *Earth, Planets Sp.* **60**, 13–20 (2008).

23.   Scheeres, D. J. *et al.* The dynamic geophysical environment of (101955) Bennu based on OSIRIS-REx measurements. *Nat. Astron.*, in press.

24.   Lee, P. *et al.* Ejecta blocks on 243 Ida and on other asteroids. *Icarus* **120**, 87–105 (1996).

25.   Michel, P., Benz, W., Tanga, P. & Richardson, D. C. Collisions and Gravitational Reaccumulation: Forming Asteroid Families and Satellites. *Science* **294**, 1696–1700 (2001).

26.   Delbó, M. *et al.* Thermal fatigue as the origin of regolith on small asteroids. *Nature* **508**, 233–236 (2014).

27.   Opeil, C. P., Consolmagno, G. J., Safarik, D. J. & Britt, D. T. Stony meteorite thermal properties and their relationship with meteorite chemical and physical states. *Meteorit. Planet. Sci.* **47**, 319–329 (2012).

28.   Müller, T. G., Sekiguchi, T., Kaasalainen, M., Abe, M. & Hasegawa, S. Thermal infrared observations of the Hayabusa spacecraft target asteroid 25143 Itokawa. *Astron. Astrophys.* **443**, 347–355 (2005).

29.   Rodgers, D. J., Ernst, C. M., Barnouin, O. S., Murchie, S. L. & Chabot, N. L. Methodology for finding and evaluating safe landing sites on small bodies. *Planet. Space Sci.* **134**, 71–81 (2016).

30.   Müller, T. G. *et al.* Hayabusa-2 mission target asteroid 162173 Ryugu (1999 JU 3): Searching for the object's spin-axis orientation. *Astron. Astrophys.* **599**, A103 (2017).

31.   Sugita, S. The geomorphology, color, and thermal properties of Ryugu: Implications for parent-body processes. *Science*, in review.

32.   Saito, J. *et al.* Detailed Images of Asteroid 25143 Itokawa from Hayabusa. *Science* **312**, 1341–1344 (2006).

33.   Murchie, S. *et al.* Color Variations on Eros from NEAR Multispectral Imaging. *Icarus* **155**, 145–168 (2002).

34.   Riner, M. A., Robinson, M. S., Eckart, J. M. & Desch, S. J. Global survey of color variations on 433 Eros: Implications for regolith processes and asteroid environments. *Icarus* **198**, 67–76 (2008).

35.   Lantz, C., Binzel, R. P. & DeMeo, F. E. Space weathering trends on carbonaceous asteroids: A possible explanation for Bennu's blue slope? *Icarus* **302**, 10–17 (2018).

36.   Thompson, M. S., Loeffler, M. J., Morris, R. V., Keller, L. P., & Christoffersen, R. Spectral and chemical effects of simulated space weathering of the Murchison CM2 carbonaceous chondrite. *Icarus* **319**, 499–511 (2019).

37.   Johnson, T. V. & Fanale, F. P. Optical properties of carbonaceous chondrites and their relationship to asteroids. *J. Geophys. Res.* **78**, 8507–8518 (1973).

38.   Biele, J., Kührt, E., Senshu, H., Sakatani, N., Ogawa, K., Hamm, M., Grott, M., Okada, T., Arai, T. Effects of Dust Layers on Thermal Emission from an Asteoridss's Surface. *Prog. Earth Planet. Sci.*

39.   Sanchez, J. A. *et al.* Phase reddening on near-Earth asteroids: Implications for mineralogical analysis, space weathering and taxonomic classification. *Icarus* **220**, 36–50 (2012).

40. Li, J. *et al.* Spectrophotometric modeling and mapping of Ceres. *Icarus* **322**, 144–167 (2019).

41. Muinonen, K. *et al.* Asteroid photometric and polarimetric phase curves: Joint linear-exponential modeling. *Meteorit. Planet. Sci.* **44**, 1937–1946 (2009).

42. Pilorget, C., Fernando, J., Ehlmann, B. L., Schmidt, F. & Hiroi, T. Wavelength dependence of scattering properties in the VIS-NIR and links with grain-scale physical and compositional properties. *Icarus* **267**, 296–314 (2016).

43. Rozitis, B. The surface roughness of (433) Eros as measured by thermal-infrared beaming. *Mon. Not. R. Astron. Soc.* **464**, 915–923 (2017).

44. Rozitis, B., Green, S. F., MacLennan, E. & Emery, J. P. Observing the variation of asteroid thermal inertia with heliocentric distance. *Mon. Not. R. Astron. Soc.* **477**, 1782–1802 (2018).

45. Rozitis, B. & Green, S. F. Physical characterisation of near-Earth asteroid (1620) Geographos. *Astron. Astrophys.* **568**, A43 (2014).

46. Spencer, J. R. A rough-surface thermophysical model for airless planets. *Icarus* **83**, 27–38 (1990).

47. Rozitis, B. & Green, S. F. Directional characteristics of thermal-infrared beaming from atmosphereless planetary surfaces - a new thermophysical model. *Mon. Not. R. Astron. Soc.* **415**, 2042–2062 (2011).

48. Jaumann, R. *et al.* Surface Geomorphology of Near Earth Asteroid (162173) Ryugu from in-situ Observations: First Results from the MASCOT Camera. Abstract P21A-03 presented at 2018 Fall Meeting, AGU, Washington, D.C., 10-14 Dec.

49. Nakamura, A. M., Fujiwara, A. & Kadono, T. Velocity of finer fragments from impact. *Planet. Space Sci.* **42**, 1043–1052 (1994).

50. Hanuš, J., Delbo, M., Ďurech, J. & Alí-Lagoa, V. Thermophysical modeling of main-belt asteroids from WISE thermal data. *Icarus* **309**, 297–337 (2018).

51. Nagao, K. *et al.* Irradiation History of Itokawa Regolith Material Deduced from Noble Gases in the Hayabusa Samples. *Science* **333**, 1128–1131 (2011).

52. Scheeres, D. J., Hartzell, C. M., Sánchez, P. & Swift, M. Scaling forces to asteroid surfaces: The role of cohesion. *Icarus* **210**, 968–984 (2010).

53. Lauretta, D. S. *et al.* OSIRIS-REx: Sample Return from Asteroid (101955) Bennu. *Space Sci. Rev.* **212**, 925–984 (2017).

Corresponding Authors

Daniella DellaGiustina, danidg@lpl.arizona.edu
Joshua Emery, jemery2@utk.edu

Acknowledgements

Author Contributions

D.N.D. leads the Image Processing Working Group (IPWG). J.P.E. leads the Thermal Analysis Working Group (TAWG). Both led the analysis and paper writing efforts. M.A.B., C.A.B., K.N.B., H.C., J.d.L., C.Y.D.d'A., S.F., D.R.G., C.H., E.S.H., H.H.K., T.K., L.L.C., J.-Y.L., J.L., J.L.R.G., P.M., M.N., M.P., D.C.R., B.R., P.H.S., E.T., C.A.T., and X.-D.Z. contributed to the image processing analysis of MapCam images. O.S.B., K.J.B., C.A.B., D.R.G., and C.H. contributed to the production of the global mosaic. E.A., R.-L.B., O.S.B., C.A.B., E.B.B., W.F.B., K.N.B., H.C., H.C.C.Jr., M.D., M.D., C.M.E., E.R.J., P.M., J.M., M.N., M.P., A.R., S.R.S., E.T., and K.J.W. contributed to the interpretation of the boulder size frequency distribution. B.E.C., J.D.P.D., C.Y.D.d'A., S.F., D.R.G., C.H., E.S.H., J.-Y.L., B.R., N.S., A.A.S., P.H.S., and X.-D.Z. contributed to the interpretation of the photometric model. E.A., R.-L.B., J.L.B., O.S.B., R.P.B., W.F.B., N.B., P.R.C., B.C.C., M.D., C.M.E., V.E.H., E.S.H., E.R.J., T.K., L.F.L., J.M., M.N., M.P., D.C.R., B.R., A.R., S.R.S., M.A.S., A.A.S., E.T., C.A.T., and K.J.W. contributed to the interpretation of thermophysical measurements. N.B., P.R.C., L.F.L., B.R., and M.A.S. contributed to the analysis or calibration of thermal data. D.N.D., C.Y.D.d'A., J.P.E., D.R.G., V.E.H., C.H., L.F.L., D.C.R., B.R., and A.A.S. contributed to the planning of observations. K.J.B., C.Y.D.d'A., D.R.G., E.S.H., B.R., N.S., P.H.S., and X.-D.Z. contributed to the calibration of image data. D.S.L. leads the mission and contributed significantly to the analysis. C.W.V.W. contributed substantially to the content and writing of the paper. The entire OSIRIS-REx Team made the encounter with Bennu possible.

Author information

D.N. DellaGiustina, Lunar and Planetary Laboratory, University of Arizona, 1415 N 6th Ave, Tucson, AZ 85705, USA.

J.P. Emery, Department of Earth and Planetary Sciences, University of Tennessee, Knoxville, TN 37996, USA.

D.R. Golish, Lunar and Planetary Laboratory, University of Arizona, 1415 N 6th Ave, Tucson, AZ 85705, USA.

B. Rozitis, School of Physical Sciences, Open University, Milton Keynes MK7 6AA, UK.

C.A. Bennett, Lunar and Planetary Laboratory, University of Arizona, 1415 N 6th Ave, Tucson, AZ 85705, USA.

K.N. Burke, Lunar and Planetary Laboratory, University of Arizona, 1415 N 6th Ave, Tucson, AZ 85705, USA.

R.-L. Ballouz, Lunar and Planetary Laboratory, University of Arizona, 1415 N 6th Ave, Tucson, AZ 85705, USA.

K.J. Becker, Lunar and Planetary Laboratory, University of Arizona, 1415 N 6th Ave, Tucson, AZ 85705, USA.

P.R. Christensen, Department of Geological Science, Arizona State University, Tempe, AZ 85281, USA.

C.Y. Drouet d'Aubigny, Lunar and Planetary Laboratory, University of Arizona, 1415 N 6th Ave, Tucson, AZ 85705, USA.

V.E. Hamilton, Southwest Research Institute, 1050 Walnut St Suite 300, Boulder, CO 80302, USA.

D.C. Reuter, NASA Goddard Space Flight Center, Greenbelt, MD 20771, USA.

B.R. Rizk, Lunar and Planetary Laboratory, University of Arizona, 1415 N 6th Ave, Tucson, AZ 85705, USA.

A.A. Simon, NASA Goddard Space Flight Center, Greenbelt, MD 20771, USA.

E. Asphaug, Lunar and Planetary Laboratory, University of Arizona, 1415 N 6th Ave, Tucson, AZ 85705, USA.

J.L. Bandfield, Space Science Institute, 4750 Walnut St Suite 205, Boulder, CO 80301, USA.

O.S. Barnouin, The Johns Hopkins University Applied Physics Laboratory, 11100 Johns Hopkins Road, Laurel, MD 20723, USA.

M.A. Barucci, LESIA-Observatoire de Paris, CNRS, PSL, Sorbonne Université, Université Paris-Diderot, 92195 Meudon Principal Cedex, France.

B. Bierhaus, Lockheed-Martin Space Systems Company, 12257 S Wadsworth Blvd, Littleton, CO 80201, USA.

R.P.B. Binzel, Massachusetts Institute of Technology

W. F. Bottke, Southwest Research Institute, 1050 Walnut St Suite 300, Boulder, CO 80302, USA.

N. Bowles, University of Oxford

H. Campins, Department of Physics, University of Central Florida, Orlando, FL 32816, USA.

B. C. Clark, Space Science Institute, 4750 Walnut St Suite 205, Boulder, CO 80301, USA.

B. E. Clark, Department of Physics and Astronomy, Ithaca College, Ithaca, NY 14850, USA.

H. C. Connolly Jr., Department of Geology, School of Earth & Environment, Rowan University

M. Daly, York University

J. de Leon, Instituto de Astrofísica de Canarias, C/Vía Láctea s/n, E-38205 La Laguna, Tenerife, Spain / Departamento de Astrofísica, Universidad de La Laguna, E-38206 La Laguna, Tenerife, Spain

M. Delbó, Université Côte d'Azur, Observatoire de la Côte d'Azur, CNRS, France.

J.D.P. Deshapriya, LESIA-Observatoire de Paris, CNRS, PSL, Sorbonne Université, Université Paris-Diderot, 92195 Meudon Principal Cedex, France

C.M. Elder, Jet Propulsion Laboratory, 4800 Oak Grove Dr, Pasadena, CA 91109, USA.

S. Fornasier, LESIA-Observatoire de Paris, CNRS, PSL, Sorbonne Université, Université Paris-Diderot, 92195 Meudon Principal Cedex, France

C. Hergenrother, Lunar and Planetary Laboratory, University of Arizona, 1415 N 6th Ave, Tucson, AZ 85705, USA.

E.S. Howell, Lunar and Planetary Laboratory, University of Arizona, 1415 N 6th Ave, Tucson, AZ 85705, USA.

E.R. Jawin, Smithsonian Institution National Museum of Natural History

H.H. Kaplan, Southwest Research Institute, 1050 Walnut St Suite 300, Boulder, CO 80302, USA.

D.S. Lauretta, Lunar and Planetary Laboratory, University of Arizona, 1415 N 6th Ave, Tucson, AZ 85705, USA.

L. Le Corre, Planetary Science Institute, 1700 E Fort Lowell Suite 106, Tucson, AZ 85719, USA.

J.-Y. Li, Planetary Science Institute, 1700 E Fort Lowell Suite 106, Tucson, AZ 85719, USA.

J. Licandro, Instituto de Astrofísica de Canarias, C/Vía Láctea s/n, E-38205 La Laguna, Tenerife, Spain / Departamento de Astrofísica, Universidad de La Laguna, E-38206 La Laguna, Tenerife, Spain

L.F. Lim, NASA Goddard Space Flight Center, Greenbelt, MD 20771, USA.

J. L. Rizos Garcia, Instituto de Astrofísica de Canarias, C/Vía Láctea s/n, E-38205 La Laguna, Tenerife, Spain / Departamento de Astrofísica, Universidad de La Laguna, E-38206 La Laguna, Tenerife, Spain

P. Michel, Université Côte d'Azur, Observatoire de la Côte d'Azur, CNRS, Laboratoire Lagrange

J. Molaro, Jet Propulsion Laboratory, 4800 Oak Grove Dr, Pasadena, CA 91109, USA.

M. Nolan, Lunar and Planetary Laboratory, University of Arizona, 1415 N 6th Ave, Tucson, AZ 85705, USA.

M. Pajola, Istituto Nazionale di Astrofisica, Astronomical Observatory of Padova, 35122 Padova PD, Italy.

M. Popescu, Instituto de Astrofísica de Canarias, C/Vía Láctea s/n, E-38205 La Laguna, Tenerife, Spain / Departamento de Astrofísica, Universidad de La Laguna, E-38206 La Laguna, Tenerife, Spain

A. Ryan, Université Côte d'Azur, Observatoire de la Côte d'Azur, CNRS, France.

S.R. Schwartz, Lunar and Planetary Laboratory, University of Arizona, 1415 N 6th Ave, Tucson, AZ 85705, USA.

N. Shultz, Lunar and Planetary Laboratory, University of Arizona, 1415 N 6th Ave, Tucson, AZ 85705, USA.

M.A. Siegler, Southern Methodist University

P.H. Smith, Lunar and Planetary Laboratory, University of Arizona, 1415 N 6th Ave, Tucson, AZ 85705, USA.

E. Tatsumi, Department of Earth and Planetary Science, The University of Tokyo

C.A. Thomas, Northern Arizona University

K.J. Walsh, Southwest Research Institute, 1050 Walnut St Suite 300, Boulder, CO 80302, USA.

C.W.V. Wolner, Lunar and Planetary Laboratory, University of Arizona, 1415 N 6th Ave, Tucson, AZ 85705, USA.

X.-D. Zou, Planetary Science Institute, 1700 E Fort Lowell Suite 106, Tucson, AZ 85719, USA.

Main figure legends

Figure 1. Resolved phase curves of Bennu.
a, Global reflectance values of Bennu's surface as a function of phase angle, which convey Bennu's photometric behavior. We fit these data to an exponential phase function for each MapCam band. For clarity, the phase function of the spectral average is shown as a dashed line.
b, Spectral dependence is observed when reflectance for the b' (473 nm), w (698 nm), and x (847 nm) bands are plotted relative to the v band (550 nm) at 0° phase angle. The positive slope in the w and x data, and negative slope in the b' data, demonstrate phase reddening.

Figure 2. Asteroid Bennu imaged by the OSIRIS-REx Camera Suite
a, Bennu whole-disk mosaics. PolyCam images from 2 December 2018 are combined to show four sides of Bennu as mosaics of the whole disk. When view from left to right to these data illustrate one rotation of Bennu. The phase angles of the images are between 47.72° and 51.91° with pixel scales between 0.509 and 2.926 m/pixel.
b, Global equirectangular map. PolyCam images acquired 1 December 2018 with phase angles between 33.22° and 35.76° and pixel scales between 0.743 and 3.866 m/pixel, with the addition of MapCam images from December 13, 2018 are projected and mosaicked into an equirectangular map of Bennu. The MapCam images have a phase angle range of 38.15° to 52.01° and a pixel scale from 1.331 to 1.885 m/pixel. North is defined as the +Z pole.

Figure 3. Global cumulative size-frequency distribution of boulders.
Bennu's global cumulative size frequency distribution of boulders plotted in logarithmic space. The data presented here are considered complete to >8 m (see methods). Note the break in trend for boulders in the 20- to 40-m-diameter range. There is a distinct lack of boulders with diameters in the ranges of 25 to 30 m and 33 to 43 m. Light blue data points represent individual boulder diameters, while the red line represents the best fit power-law slope.

Figure 4. Albedo Trends among Bennu's boulders.
a. Boulders on Bennu: Normal albedo vs. size. The brightest boulders have smaller diameters. The completeness limit of the global distribution of boulders and the global average albedo of Bennu are shown for context.
b. CSFD per albedo. Bennu's CSFD of boulders per average albedo and bright albedo (> 6.8%) in logarithmic space. While small numbers influence the power-law index for the bright boulders, these data suggest that the bright boulders have a different size-frequency distribution than the average-albedo boulders. Light blue data points represent the individual diameters of bright boulders, and dark blue points represent the individual diameters of average-to-dark boulders. The red lines associated with each data set represent their best fit power-law slope.

Figure 5. Evidence of in situ boulder disaggregation.
A boulder (approximate coordinates: 45° latitude, 110° longitude) that appears to be degrading into its constituent clasts. This image was acquired with PolyCam and has a phase angle of 51.33° and a pixel scale of 0.643 m/pixel.

Figure 6. Dark diffuse units.
The inset shows one of many dark diffuse units on Bennu. Low-albedo (~3.4%) material blankets underlying terrain with a global average albedo. The central boulder mantled by dark material is at approximately –65° latitude, 32° longitude. The image has a low phase angle of 4.292° and pixel scale of 3.546 m/pixel. This image has been stretched to highlight areas of dark material.

Methods

Calibration of OCAMS images.

OCAMS images are processed by a calibration pipeline to be corrected for known sources of noise and converted to physical units. The corrections include bias and dark subtraction, charge smear removal, and flat fielding. The pipeline removes noise using algorithms and data generated by a combination of ground-based and in-flight calibrations. The conversion to physical units is in terms of reflectance (i.e. radiance factor or I/F). All image data used in this analysis are described in terms of reflectance.

The absolute accuracy of the radiometric calibration is set by the in-flight calibration using images of the Moon taken during the OSIRIS-REx Earth Gravity Assist (EGA). We compare these images, taken with each of the cameras and with each of MapCam's filters, with images taken by the RObotic Lunar Observatory (ROLO [54]). We use the ROLO bands that most closely match the OCAMS filters: 475 nm for b´, 553 nm for v, 703 nm for w, 865 nm for x, and 665 nm for pan. We scale the ROLO data to match the phase angle of the OCAMS EGA images, ~42°, using the ROLO photometric model of the lunar surface.

We register the ROLO data to their backplanes and project them into a common equal-area map and then back-project the data into OCAMS camera space. Because the ROLO and OCAMS acquired their images with different illumination conditions, we photometrically correct the ROLO and OCAMS data with a McEwen model [55]. Moreover, because the ROLO and OCAMS images view different portions of the moon, we reduce the area of the OCAMS images to match ROLO images. We can then directly compare ROLO and OCAMS data by taking a ratio of the images projected into the same space. This comparison is somewhat noisy due to imperfect registration between the two images. Therefore, we calculate a histogram of the image ratio and reduce the dataset to pixels that are within two standard deviations of the mean. This reduces the noise and effectively eliminates limb pixels, which have non-physical values after photometric correction. We take the mean of the remaining pixels to produce the correction to the OCAMS radiometric calibration.

Global mosaic of Bennu.

The global mosaic of Bennu in Fig. 2 was constructed using calibrated PolyCam images in units of I/F taken on 1 December 2018 over full 4.3-hr rotational period of Bennu. The images were taken between 05:13:11 and 09:11:41 UTC when the spacecraft's distance to Bennu was between 30.3 and 31.6 km. The corresponding spatial scale of the images was between 0.41 and 0.43 m per pixel, while the phase angle of the observation changed between 33.7° and 35.7°. Additional MapCam images from 13 December 2018 were added to fill in the south pole (–Z). These images were taken between 00:47:30 and 05:04:57 UTC. Spacecraft distance was between 8.93 and 11.09 km. The pixel resolution of the images were between 1.600 and 1.885 m/pixel with phase angles between 39.3° and 56.2°.

The global mosaic was constructed using the software and methods described in DellaGiustina et al. [56]. No photometric correction was performed prior to mosaicking, however a process similar to the ISIS3 noseam application was applied to minimize the presence of seams and improve the cosmetic quality of the mosaic. Finally, some images were manually placed in areas where automatic image prioritization mosaicking scheme yielded imperfect results. All geographic coordinates in this paper use a 0-360° convention for longitude.

Boulder size-frequency distribution and albedo calculations.

OSIRIS-REx Mission Terminology defines a feature as a boulder if it has positive relief and a diameter ≥ 21 cm, a size that is consistent with the diameter of the TAGSAM annular aperture. In that Mission Terminology, "cobbles" are particles between 2 and 21 cm, and regolith fines are all particles smaller than 2 cm (i.e., ingestible by the sampling mechanism). We use this terminology through the manuscript. For the purposes of counting a boulder towards the statistical population of particles on Bennu's surface, these objects must also have a definable perimeter that is not partially buried and be characterized by the consistent presence of an elongated shadow. Accordingly, the partially exposed dark boulder outcrop at (–20° latitude, 30° longitude) is not counted within the size frequency distribution we report, as its full extent remains unknown.

Boulders in this dataset were identified across seven PolyCam images taken on 1 December 2018, covering a full rotational period of Bennu. The images were taken between 05:13:11 and 09:11:41 UTC when the spacecraft's distance to Bennu was between 30.3 and 31.6 km. The corresponding spatial scale of these images was between 0.41 and 0.43 m per pixel, while the phase angle of the observation changed between 33.7° and 35.7°.

Using the geographic information system software ArcMap, boulders were manually identified in OCAMS images using polylines. The longest axis dimension was measured; for simplicity we refer to this as boulder diameter. The position of polyline geometries are linked to the body-fixed Cartesian coordinates from OCAMS geometric backplanes, which were calculated using the ISIS3 spiceinit routine and the v13 shape model of Bennu, with an average facet size of 75 cm [3]. The polyline endpoints and the midpoint are recorded and used to calculate boulder length. This technique allows us to identify boulders on unprojected images that have not been resampled.

Reflectances for each boulder were extracted from the midpoint of each polyline to avoid shadowed pixels that often occur at measurement endpoints. Reflectances were converted to normal albedo using the Lommel-Seeliger disk function and an exponential phase function (see Resolved Photometric Modeling Methods) to correct I/F values to 0° phase angle, 0° emission angle, and 0° incidence angle (0°, 0°, 0°). Boulders with reflectances below 0.03 were not included in this analysis as manual inspection of several low reflectance boulders indicate shadowing. Likewise, boulders identified at incidence or emission angles ≥70° were excluded as reflectance values after photometric correction with a Lommel-Seeliger disk function may

become unphysical as those angles approach 90°. We consider bright boulders to be >6.8% normal albedo, which represents boulders that exceed 1σ of the mean boulder albedo for the global population of boulders presented here.

In Figure 3, we plot the global unbinned CSFD of boulders on Bennu in logarithmic space. In Figure 4b, we plot the unbinned cumulative size frequency distribution per normal albedo in logarithmic space. For each data set, we assume the number of boulders detected follows a Poisson distribution [57]. Thus, measurement uncertainty for individual boulders is captured as the square-root of the number of boulders greater than or equal to D, normalized by surface area. We use surface area of 0.786 km^2 derived from the v13 shape model [3].

Completeness limits used to determine CSFDs were estimated from the data using a statistical approach to limit individual judgement in the assessment of data completeness. Specifically, we follow the technique recommended by Clauset et al. [58] and applied to boulder size frequency distributions by DeSouza et al. [59]. Accordingly, completeness is defined as the smallest value above which the differences between the probability distributions of the measured data and a best-fit power-law model are minimized. The distance between both distributions is quantified using the Kolmogorov-Smirnov (KS) statistic. We estimated the uncertainty for each completeness limit by performing a nonparametric bootstrap. This randomly samples the measurements with replacement to produce 1000 synthetic data sets of a similar distribution, estimating the completeness limit for each, and taking the standard deviation. For the global population, we estimate a completeness limit of 8.4 ± 1.7 m, for the bright albedo population, 5.0 ± 0.5 m, and for the average albedo population, 5.1 ± 1.1 m. The difference in the completeness limits between the global boulder data set and the data sets per albedo likely indicates that multiple statistically distinct boulder populations exist at scales < 8.4 ± 1.7 m, which cannot be adequately modeled by a single power-law distribution.

The method of maximum likelihood is used to estimate the power-law index[58,59]. We estimated uncertainty in the power-law index in the same manner as the completeness limit by performing a nonparametric bootstrap. The resulting uncertainty value is the standard deviation of the synthetic data sets produced during the bootstrap. For the global population, we estimate a power-law index of -2.9 ± 0.3, for the bright albedo population, -4.4 ± 0.7, and for the average albedo population, -2.5 ± 0.2. The larger uncertainty associated with the bright population of boulder is likely a result of the relatively smaller number of boulders in this data set.

Observations and preparation of OTES and OVIRS thermal radiance.

The disk-integrated, rotationally resolved OVIRS data used in the thermal analysis were obtained on 2 and 3 November 2018. Observations began at 04:12 UTC each day. Exposure times were ~1 s, and spectra were taken continuously for ~4.35 hr (slightly more than one full rotation of Bennu). On 2 November, the spacecraft-Bennu distance, Bennu heliocentric distance, and phase angle were ~197 km, 1.041 AU, and 5.1°, and Bennu filled ~0.37 of the FOV. On 3 November, these values were ~190 km, 1.037 AU, 4.5°, and ~0.39. We began our analysis

with the L3a radiometrically corrected OVIRS radiance spectra. The OVIRS spectra of Bennu are dominated by thermal radiance at $\lambda \gtrsim 3$ µm. We restricted thermal analysis of OVIRS to $\lambda = 3.5 - 4.0$ µm, where the thermal radiance is ~8 to 25 times the reflected radiance. To isolate the thermal radiance, we estimated the reflected radiance by scaling the solar spectrum to each OVIRS measurement at ~2.1 µm and subtracted this estimate from the total measured radiance (Supplementary Fig. 8). We then binned the remaining thermal radiance to 1° rotation phase for analysis.

The disk-integrated, rotationally resolved OTES data used in the thermal analysis were obtained on 8 and 9 November 2018. Observations began at 04:13 UTC each day. Exposure times were ~2 s, and spectra were taken continuously for ~4.49 hr. On 8 November, the spacecraft-Bennu distance, Bennu heliocentric distance, and phase angle were ~162 km, 1.021 AU, and 4.5^o, and Bennu filled ~0.14 of the FOV. On 3 November, these values were ~159 km, 1.018 AU, 5.7^o, and ~0.15. Bennu was not perfectly centered in the OTES FOV, and the asymmetric filling caused calibration complications for this FTIR spectrometer[11]. For the analysis presented here, neither the absolute radiometric nor the relative spectral calibrations were completed. Analysis of the OTES disk-integrated approach phase data was therefore restricted to fitting relative thermal lightcurves of different wavelength channels independently. As with OVIRS, the relative thermal flux was binned to 1° rotation phase for analysis.

We also reanalyzed previous observations of Bennu by the Spitzer space telescope using the updated shape and spin state determined by OSIRIS-REx. Details of the Spitzer data can be found in Emery et al. [12], and results of the reanalysis can be found in the Supplementary Materials. For analysis of all thermal data, we used the shape model (v13) determined from stereophotoclinometry performed on images of Bennu taken with OCAMS[3] and the corresponding spin pole and rotation period (RA = 85.3 ± 0.2^o, Dec = -60.2 ± 0.2^o, rotation period = $4.296061 \pm 2 \times 10^{-6}$ hr). For thermal analysis, the facet size of the shape model we used was ~12 m. For topography (including boulders) larger than this scale, the effects of surface tilts, shadowing, and global self-heating are directly computed. The effects of roughness from smaller-scale topography, including smaller boulders, are included using hemispherical craters to simulate that sub-resolution-element roughness.

Thermal model and data fitting.

The thermophysical analysis reported here uses a custom code that is based on the Advanced Thermophysical Model (ATPM) of [47,60,61]. For a given set of input parameters (i.e. shape model, rotation period and pole orientation, illumination and viewing geometry, and Bond albedo/emissivity/thermal inertia values), the ATPM computes the surface temperature distribution of an asteroid by solving 1D heat conduction with a surface boundary condition that takes into account direct and multiple-scattered sunlight, and also self-shadowing and self-heating effects resulting from interfacing surfaces. Rough surface thermal-infrared beaming (i.e. re-radiation of absorbed sunlight back towards the Sun by small-scale surface roughness) is modeled by adding a fractional coverage of hemispherical craters to each shape model facet. The model flux is then computed from the model temperatures by summing the Planck

function across facets and parts of hemispherical craters that were visible to the observer at the time of the flux measurements. For the analysis of the thermal data of Bennu, surface temperature distributions and model fluxes were computed for thermal inertias that ranged from 0 to 600 J m^{-2} K^{-1} s$^{-1/2}$ in equally-spaced steps of 10 J m^{-2} K^{-1} s$^{-1/2}$. We use a Bond albedo of 0.016, based on the measured geometric albedo and phase behavior, and assume a bolometric and spectral emissivities of 0.9. The assumption of 0.9 for bolometric emissivity is typical of silicate materials at these wavelengths, and constant spectral emissivity is consistent with the low spectral contrast of Bennu in the mid-infrared (<2%) measured by OTES [11] and laboratory spectra of carbonaceous meteorites.

To derive the thermal properties of Bennu, the model fluxes were compared against the measured fluxes by varying the rotation phase (i.e. the initial rotational orientation of Bennu at the start of the flux measurements), thermal inertia, and surface roughness to find the minimum χ^2 fit of the dataset analyzed. The uncertainties of the derived thermal properties were assessed by using a Monte Carlo bootstrap method[44] that produced 100 synthetic test datasets from the uncertainties of the original dataset (i.e. including both the individual data point uncertainties and the instrument absolute calibration uncertainties). The minimum χ^2 fit was sought for each synthetic dataset, and their best fitting parameters were then averaged to give a mean and standard deviation of the overall model fit. We used this Monte Carlo bootstrap method for assessing the final uncertainties instead of a reduced-χ^2 cut-off because it more accurately takes into account the influence of systematic uncertainties introduced by the instrument absolute calibration.

Calculation of thermal skin depth and characteristic particle size.

The thermal skin depth is the depth over which the amplitude of the thermal wave decreases by e^{-1} and is given by

$$l_S \sim \frac{\Gamma}{c_p \rho} \sqrt{\frac{2}{\omega}} \tag{1}$$

where Γ is thermal inertia, c_p is heat capacity, ρ is grain density, and ω is the rate of temperature variation – the rotation rate of the asteroid in the case of the diurnal skin depth. From the measured thermal inertia and uncertainties, and given the range of heat capacities (500 to 1100 J kg^{-1} K^{-1}) and densities (2000 to 2900 kg m^{-3}), the diurnal skin depth on Bennu is 0.8 to 3.0 cm.

Analytical methods to estimate regolith particle size from thermal inertia on airless bodies use models of heat conduction across particle contacts and radiation between particles calibrated through laboratory experiments[13,62–64]. The general method consists of computing the effective regolith thermal conductivity from the measured thermal inertia, calculating a modeled effective thermal conductivity as a function of particle size considering both solid conduction and radiation terms for reasonable ranges of regolith properties and model parameters, then comparing the measured and modeled effective conductivities to find the particle size(s) where they agree. We employ the methods of Gundlach and Blum [13,62], and

Sakatani et al. [63] with calibration of the parameters ξ and ζ from Ryan [65] for a wide range (0.1 to 0.9) of possible regolith porosities (i.e., space between regolith grain, distinct from the boulder porosity discussed in the main text), in order to examine extremes of resulting particle sizes. Resulting modeled regolith particle diameters are 0.5 to 4 cm. It is important to note that these simple analytical methods assume that all regolith particle are the same size (i.e., monodisperse), which is physically unrealistic. These modeled particle sizes are therefore a thermally characteristic particle size that may not be the same as the average physical regolith particle diameter. For a power-law particle size distribution, the thermal flux is dominated by the smaller grains in the distribution. The estimates here, therefore, should not be taken to suggest that the regolith does not contain perhaps many larger particles (or boulders).

Resolved photometric modeling.

As this paper represents the first results from preliminary OSIRIS-REx data, we have opted to use empirical photometric functions due to their simple mathematical form and fewer free parameters than physically motivated models (such as Hapke, Shkuratov, etc.). When multiple scattering is not significant (i.e. for low reflectance asteroids) the disk-function and phase function can be separated in functional forms [6]. In this work, we choose to use an exponential phase function and use the Lommel-Seeliger disk function. The disk behavior of low reflectance objects (geometric albedo <0.2) has been shown to generally follow a Lommel-Seeliger scattering law [6].

To produce the phase plots shown in the main text, we processed images taken by MapCam in each of its 5 filters (b′, v, w, x, and pan [2]) during two mission phases. The first were acquired between October 29th and November 9th during OSIRIS-REx's Approach phase, during which time Bennu subtended at most 50 pixels across its diameter. These data contribute to the low end of the phase curve, between 0 and 20°. The second group was acquired during the Equatorial Pass of the Preliminary Survey phase, between 11 and 15 December. In these data, Bennu subtended between 400 and 900 pixels in MapCam's field of view, covering a range of phase angles from 45 to 90°.

Photometric statistics were calculated for each image individually by treating Bennu's surface as a global average. To identify the pixels that will contribute to the average, we apply a reflectance threshold to the images. This threshold was 0.2 for the Approach images, where Bennu's limb was not clearly defined, and 0.001 for Preliminary Survey images, where the limb was clear. Both thresholds were set by inspection to include uniformly illuminated portions of the surface, rejecting off-limb and terminator pixels. The average of the pixels that pass the appropriate threshold for a given image is the mean reflectance for that image.

To obtain photometric angles, the images are imported into USGS's ISIS3 using the data import program ocams2isis. We attach observation geometry to each image using kernels from the Spacecraft, Planet, Instrument, C-matrix, Events (SPICE) Toolkit developed by NASA's Navigation and Ancillary Information Facility [66]. We also attach the geometry from the v13 shape model to the images. The ISIS3 application phocube produces backplanes for the images, including

phase, incidence, and emission angle. We calculate the average of each of these backplanes to get the mean photometric angles for each image. A summary of these statistics (mean reflectance, phase, incidence, and emission) are compiled in an Image Photometric Data Information File (IPDIF). We smooth the data by averaging together images that fall within bins that are 1° wide in phase angle. The binned data are plotted to produce the reflectance curve shown in Figure 1.

We process the unbinned IPDIF with a photometric modeling script, written in Interactive Data Language (IDL), to fit the data against a Lommel-Seeliger model. This model includes the Lommel-Seeliger disk function, shown in Equation 2, and an exponential phase function, shown in Equation 3[6]. The modeling software solves for the free parameters β, γ, and δ; the disk function has no free parameters.

$$d(i, e) = \frac{\cos(i)}{\cos(i) + \cos(e)} \tag{2}$$

$$f(\alpha) = A_{LS} e^{\beta * \alpha + \gamma * \alpha^2 + \delta * \alpha^3} \tag{3}$$

We fit the data from each of the five filters to the model independently, using the mpfit tool in IDL. However, the variation between them is subtle; for clarity, Figure 1 depicts the phase curve of the spectral average, with fit parameters of $A_{LS} = 0.0265$; $\beta = -3.55 \times 10^{-2}$; $\gamma = 3.074 \times 10^{-4}$; and $\delta = -1.889 \times 10^{-6}$. Though the fit is generally good ($\chi^2 \sim 3 \times 10^{-5}$), we note some extreme ends of the phase angle range (due to the opposition surge, though minor, at the low phase angles; due to shadowing and high incidence angles at high phase angles). The exponential phase function used here does not perfectly capture those nuances, but represents the bulk of the surface behavior well.

Geometric albedo is estimated by extrapolating the reflectance phase curves to $0°$ phase angle. As the exponential phase curve used in our model does not have a term to account for opposition surge, we perform a linear extrapolation from 0.7-2° to the $0°$ phase angle as these data show a change in slope that departs from the best-fit exponential function.

The reflectance ratio in Fig. 1 is calculating by dividing the binned reflectance data for the b', w, and x filters by the data from the v filter. We further normalize the data to the v filter at 0° phase and plot them as a function of phase to illustrate the reddening that occurs at high phase. Taking the ratio of the data eliminates the need to track absolute radiometry uncertainty. However, a relative uncertainty of ~0.5% remains due to the sub-spacecraft position and the point in Bennu's orbit at which the image data were acquired. These two factors affect Bennu's apparent reflectance due to changes Bennu's projected area and its albedo variation.
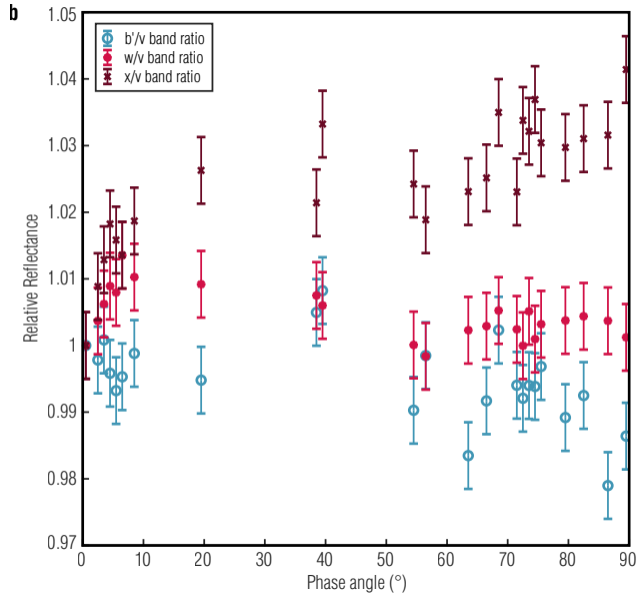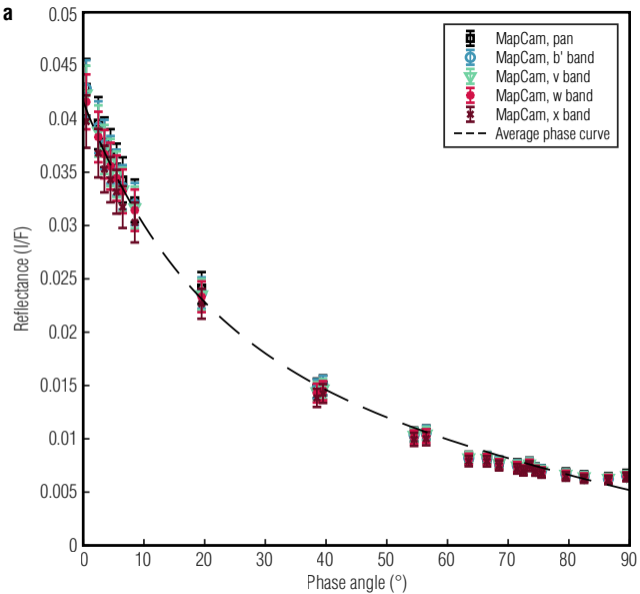
Data Availability

The data that support the plots within this paper and other findings of this study are available from the corresponding author upon reasonable request. Raw (L0) through calibrated (L2, L3)
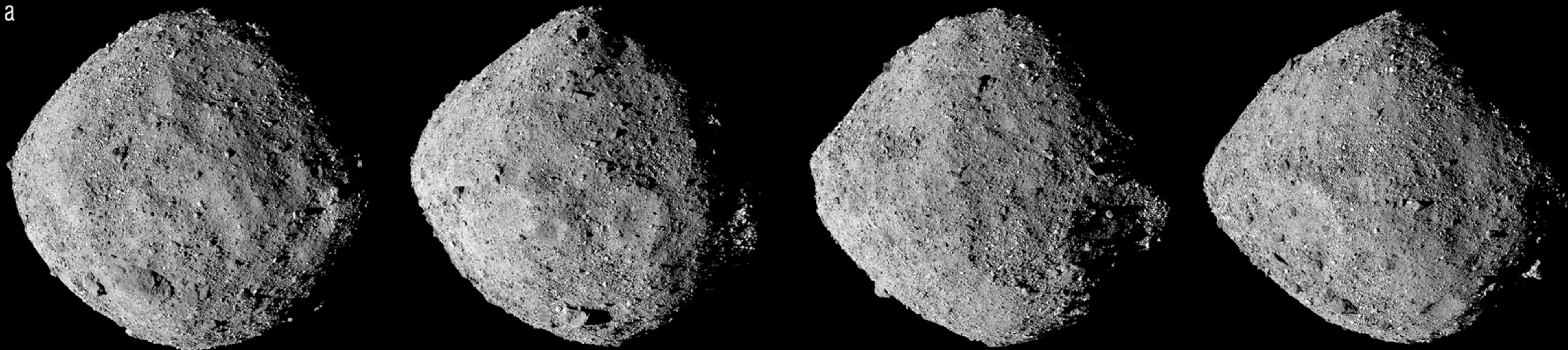
OCAMS, OVIRS, and OTES data will be available via the Small Bodies Node of the Planetary Data System (PDS) (https://pds-smallbodies.astro.umd.edu/). Data are released to the PDS according to the schedule provided in the OSIRIS-REx Data Management Plan found in the OSIRIS-REx PDS archive. Image mosaics and photometric models will be available in the PDS 1 year after departure from the asteroid.
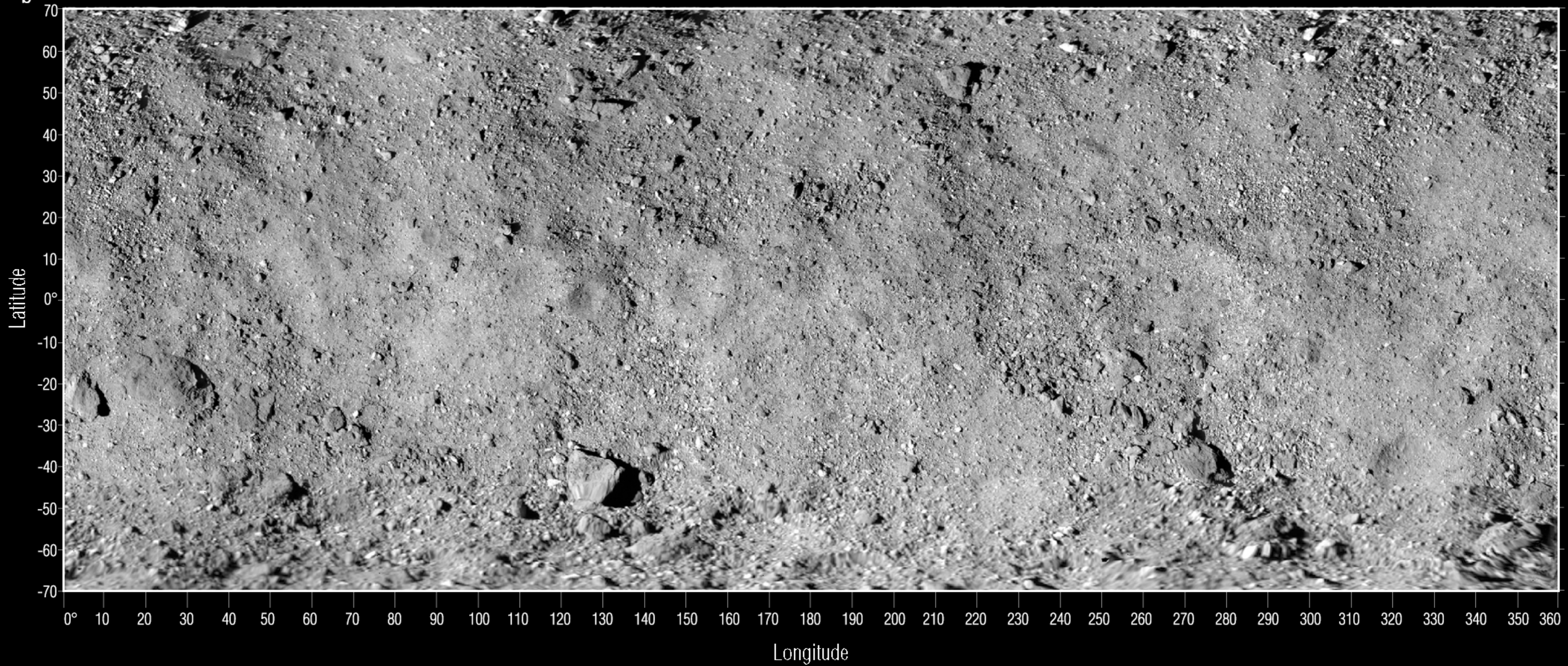
Additional references only in the Methods

54. Kieffer, H. H. & Stone, T. C. The Spectral Irradiance of the Moon. *Astron. J.* **129**, 2887–2901 (2005).
55. McEwen, A. S. A Precise Lunar Photometric Function. *Lunar and Planetary Science*. **27**, 841–842 (1996).
56. DellaGiustina, D. N. *et al.* Overcoming the Challenges Associated with Image-Based Mapping of Small Bodies in Preparation for the OSIRIS-REx Mission to (101955) Bennu. *Earth Sp. Sci.* **5**, 929–949 (2018).
57. Uni-, W. *et al.* Standard techniques for presentation and analysis of crater size-frequency data. *Icarus* **37**, 467–474 (1979).
58. Clauset, A., Shalizi, C. R. & Newman, M. E. J. Power-Law Distributions in Empirical Data. *SIAM Rev.* **51**, 661–703 (2009).
59. DeSouza, I., Daly, M. G., Barnouin, O. S., Ernst, C. M. & Bierhaus, E. B. Improved techniques for size-frequency distribution analysis in the planetary sciences: Application to blocks on 25143 Itokawa. *Icarus* **247**, 77–80 (2015).
60. Rozitis, B. & Green, S. F. The influence of rough surface thermal-infrared beaming on the Yarkovsky and YORP effects. *Mon. Not. R. Astron. Soc.* **423**, 367–388 (2012).
61. Rozitis, B. & Green, S. F. The influence of global self-heating on the Yarkovsky and YORP effects. *Mon. Not. R. Astron. Soc.* **433**, 603–621 (2013).
62. Gundlach, B. & Blum, J. Outgassing of icy bodies in the Solar System – II: Heat transport in dry, porous surface dust layers. *Icarus* **219**, 618–629 (2012).
63. Sakatani, N. *et al.* Thermal conductivity model for powdered materials under vacuum based on experimental studies. *AIP Adv.* **7**, (2017).
64. Sakatani, N., Ogawa, K., Arakawa, M. & Tanaka, S. Thermal conductivity of lunar regolith simulant JSC-1A under vacuum. *Icarus* **309**, 13–24 (2018).
65. Ryan, A. J. Heat and Mass Transfer on Planetary Surfaces. Thesis, Arizona State University, 2018.
66. Acton, C., Bachman, N., Semenov, B. & Wright, E. A look towards the future in the handling of space science mission geometry. *Planet. Space Sci.* **150**, 9–12 (2018).
67. Gault, B. D. E., Shoemaker, E. M. & Moore, H. J. *Spray Ejected From The Lunar Surface By Meteoroid Impact* (NASA, 1963).
68. Moore, H.J. Large Blocks Around Lunar Craters. in *Analysis of Apollo 10: Photography and Visual Observations* (NASA, 1971).
69. Bart, G. D. & Melosh, H. J. Using lunar boulders to distinguish primary from distant secondary impact craters. *Geophys. Res. Lett.* **34**, L07203 (2007).

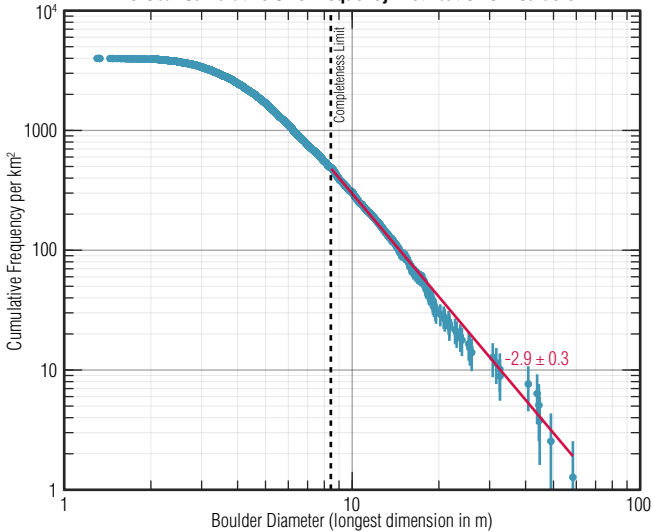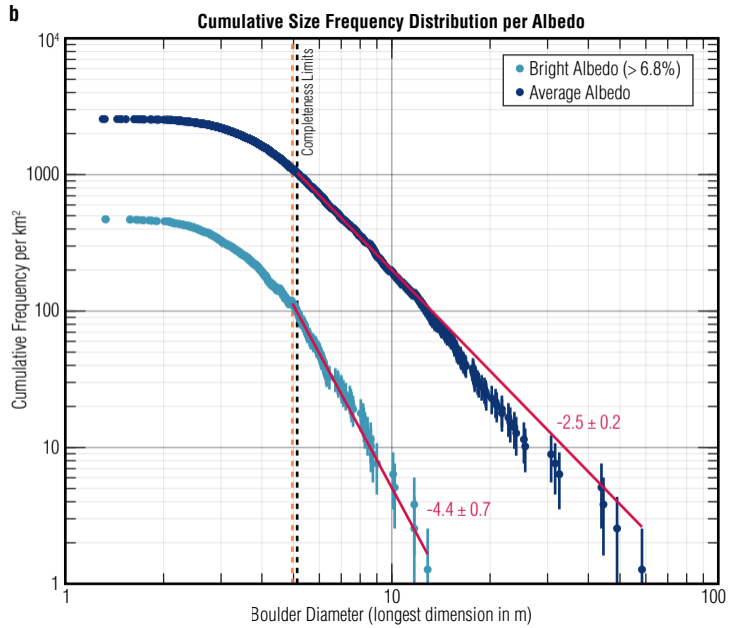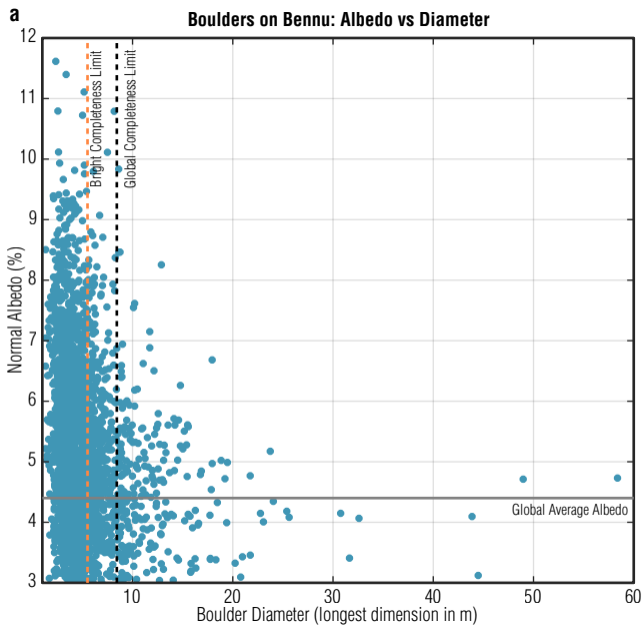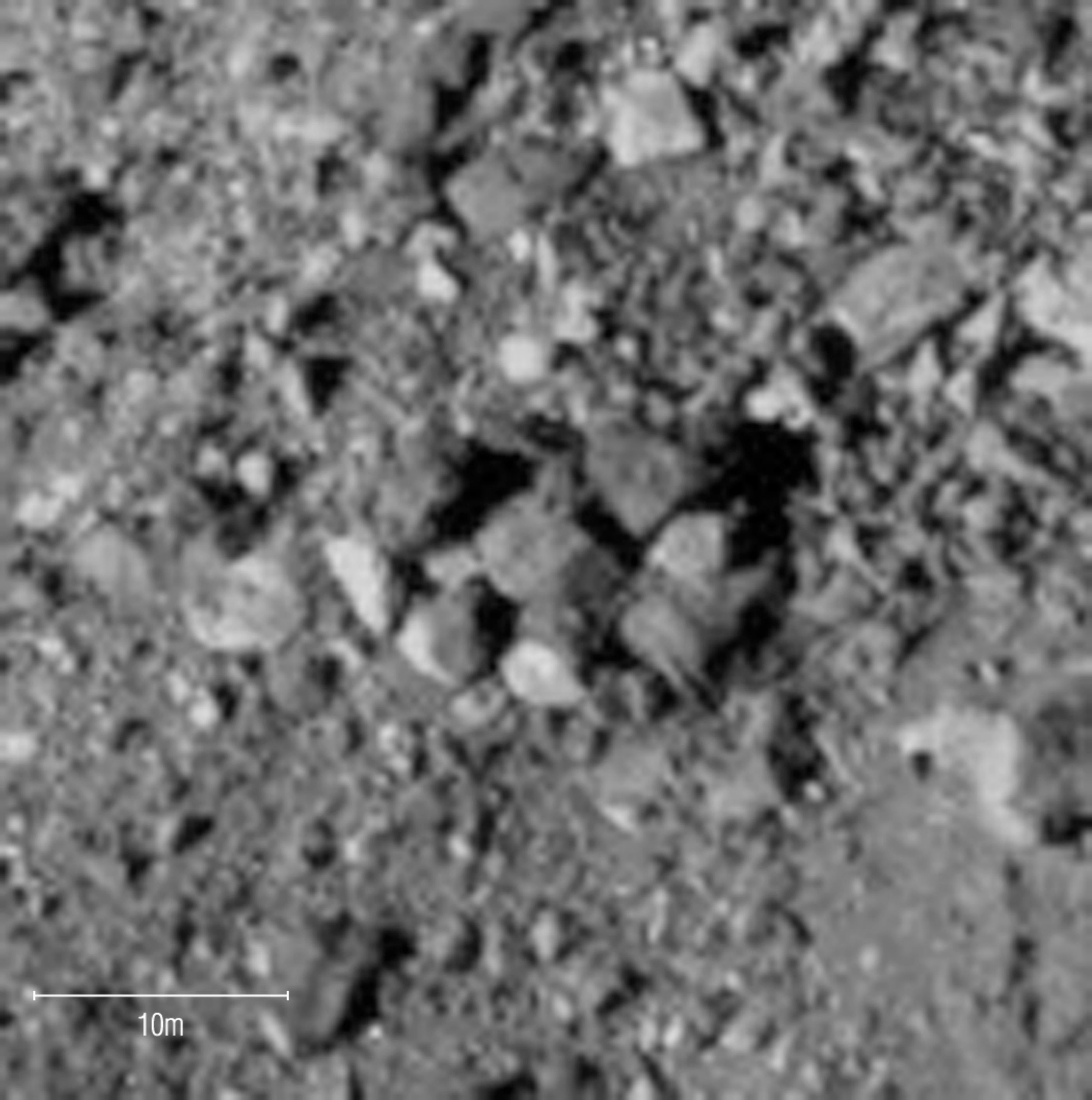**a**

Reflectance (I/F) vs Phase angle (°)

Legend:
- MapCam, pan
- MapCam, b' band
- MapCam, v band
- MapCam, w band
- MapCam, x band
- Average phase curve

b

Relative Reflectance vs Phase angle (°)

Legend:
- b'/v band ratio
- w/v band ratio
- x/v band ratio

a

b

Global Cumulative Size Frequency Distribution of Boulders

Cumulative Frequency per km² (y-axis, ranging from 1 to 10⁴)

Boulder Diameter (longest dimension in m) (x-axis, ranging from 1 to 100)

Completeness Limit

-2.9 ± 0.3

a Boulders on Bennu: Albedo vs Diameter

Normal Albedo (%) vs Boulder Diameter (longest dimension in m)

Bright Completeness Limit

Global Completeness Limit

Global Average Albedo

b Cumulative Size Frequency Distribution per Albedo

Cumulative Frequency per km² vs Boulder Diameter (longest dimension in m)

Completeness Limits

- Bright Albedo (> 6.8%)
- Average Albedo

−2.5 ± 0.2

−4.4 ± 0.7

10m

10m

Supplementary Materials

Motivation for thermal observations and analysis. Thermal analysis of Bennu is an important objective of the OSIRIS-REx mission. Global and local determination of thermophysical properties of the surface provides temperature predictions for spacecraft safety constraints (the highest surface temperatures pose a potential risk of overheating the spacecraft during sampling), informs the determination of the regolith particle size for sampleability considerations, and enables assessment of mineral and volatile thermal stability for considerations of the relative scientific value of different potential sample sites. Testing and refining the theory of the Yarkovsky effect is also a primary objective of the mission.

With these objectives in mind, we carefully planned a large number of thermal observations during the ~1.5 years of proximity operations before sampling the surface. The Approach-phase observations described here enable direct comparisons to previous Spitzer Space Telescope observations of Bennu and provide the first direct test of the Yarkovsky effect[23]. Data from the Preliminary Survey mission phase in December 2018 provided the first disk-resolved thermal data of Bennu.

Reanalysis of Spitzer space telescope observations. We began the thermal study with a reanalysis of previous thermal observations of Bennu from the Spitzer Space Telescope[12] using the updated shape and spin information from OSIRIS-REx. The Spitzer data consist of 11 point thermal lightcurves at six different wavelengths: 3.6, 4.5, 5.8, 8.0, 16, and 22 μm. The Spitzer observations occurred when Bennu was 1.124–1.143 AU from the Sun, 0.506–0.533 AU from Spitzer, and at phase angles of 61.7–63.5°. Using the shape model derived from radar observations[20], Emery et al. [12] reported a thermal inertia of 310 ± 70 J m^{-2} K^{-1} s$^{-1/2}$, with no rotational variations greater than the reported uncertainty. Our updated analysis with the OSIRIS-REx shape model provides a better fit to the Spitzer data, as illustrated in Supplementary Figure 1 for the 8-μm Spitzer lightcurve. The resulting thermal inertia of 370 ± 20 J m^{-2} K^{-1} s$^{-1/2}$ is within the uncertainties of the previously reported value. We find a fairly rough surface, characterized by RMS surface slopes of $37 \pm 2°$ (a fraction 0.58 ± 0.06 of the surface covered in hemispherical model craters). The new analysis places tighter constraints on rotational variations of thermal inertia (at the global scale) at the level of the new, smaller uncertainties.
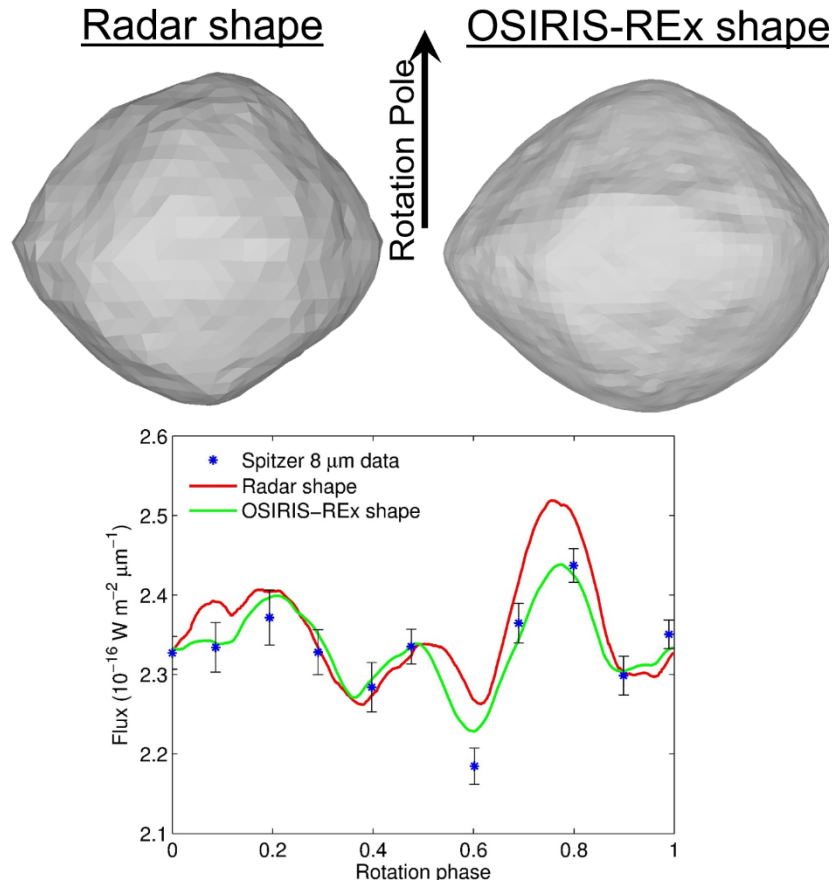
Supplementary Figure 1. Reanalysis of Spitzer data with OSIRIS-REx shape. The shapes of Bennu derived from radar observations[20] and from stereophotoclinometry applied to images of Bennu from OSIRIS-REx are compared at the top of the image. The shape derived from OSIRIS-REx data is slightly more oblate than the radar shape model. The bottom plot shows thermal fluxes of Bennu at 8 μm measured by the Spitzer space telescope (blue points) along with the best fit model thermal lightcurve using the radar shape (red curve) and the OSIRIS-REx shape model (green curve). The OSIRIS-REx shape model produces a significantly improved fit to the Spitzer measurements.

Thermal analysis of OTES and OVIRS approach phase observations. We focused our analysis of the OTES approach-phase data on fitting thermal light curves within individual spectral channels. Because OTES is a Fourier transform interferometer, observations of a target that does not fill and is not centered in the field of view are particularly difficult to properly calibrate. As a result, the absolute flux and relative spectral response for these disk-integrated observations are not well calibrated. OTES was designed and calibrated for disk-resolved observations, and is working very well to design specifications; this complication does not affect observations when Bennu fills the FOV (e.g., the preliminary survey phase observations in December 2018). For the analysis of the disk-integrated data presented here, we therefore focus on the relative time-series data within individual spectral channels. At the low phase angle of the OTES observations (~5°), the relative thermal lightcurves are strongly controlled by the shape and surface roughness; thermal inertia has a very weak effect. As illustrated in

Supplementary Figure 2a, a high surface roughness of ~43° is required to fit the OTES relative thermal lightcurves.

The thermal radiance from OVIRS data provides strong new constraints on both thermal inertia and roughness of Bennu. Using the OSIRIS-REx-derived shape model and rotation state described in Methods, we are able to accurately reproduce the measured OVIRS thermal radiance, as illustrated in Supplementary Figure 2b. Fitting the OVIRS thermal radiance light curves and spectra in the 3.5 to 4.0 μm, we find a thermal inertia of 350 ± 20 J m^{-2} K^{-2} s$^{-1/2}$ and surface roughness characterized by RMS slope of 43 ± 1° (0.77 ± 0.04 coverage of hemispherical model craters), in agreement with analysis of the Spitzer data and the OTES data.
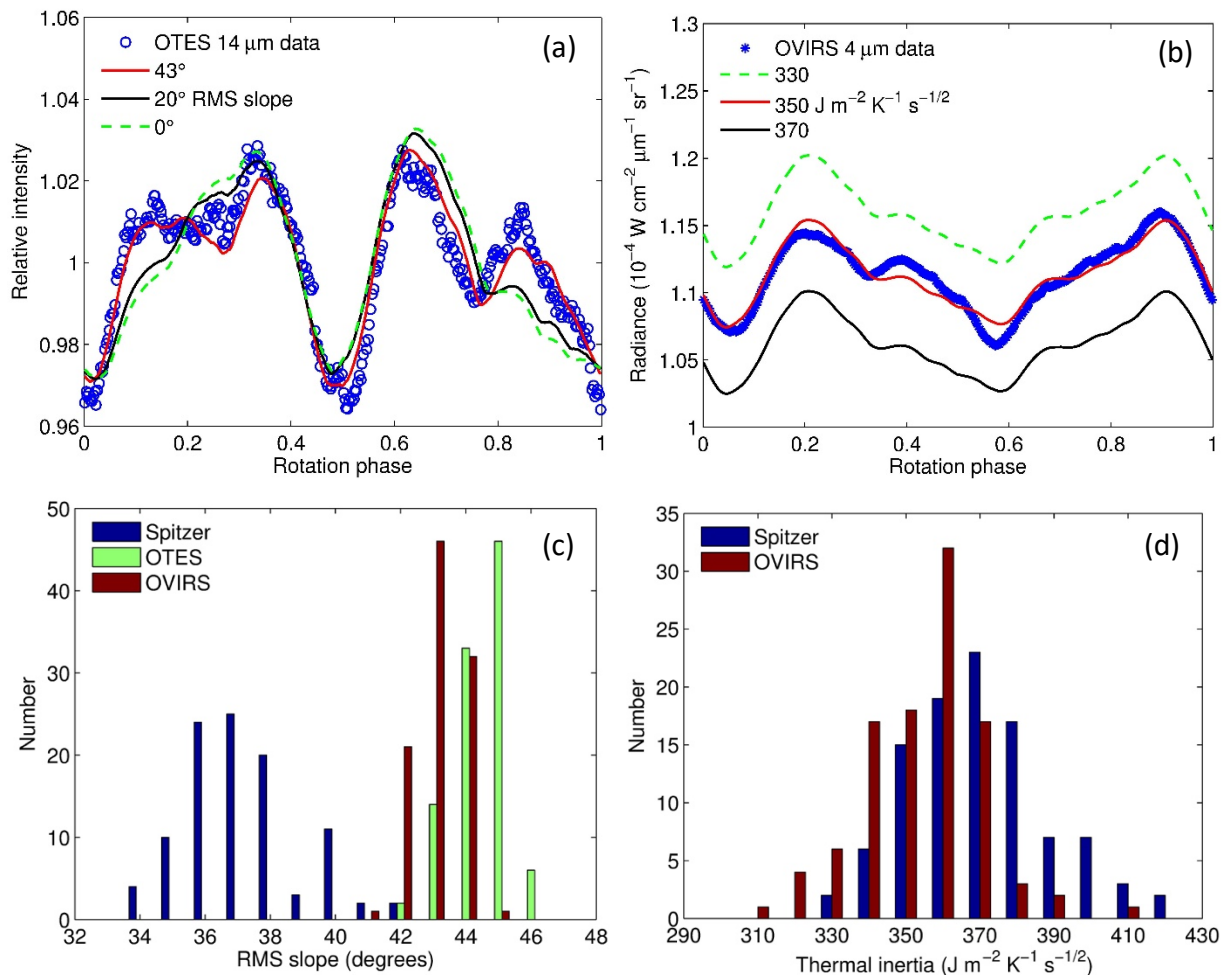
Supplementary Figure 2. a, Thermal model fits to the relative thermal light curve measured by OTES at 14 μm. The OTES data (blue circles) are normalized to the mean signal in this channel and binned to 1° rotational phase. The curves show model fits with different surface roughness for a thermal inertia of 350 J m^{-2} K^{-1} s$^{-1/2}$. A rough surface is required to fit the OTES light curve. Other wavelength channels give similar results. ***b,*** Thermal model fits to the thermal light curve measured by OVIRS at 4 μm. The data are properly calibrated in radiance units in this case. The thermal radiance has been isolated as described in the Methods. The curves show model fits with different thermal inertias for a surface roughness of 43° RMS slope, illustrating the strong constraint on thermal inertia provided by the OVIRS data. ***c,*** Histograms of roughness solutions from the Monte Carlo bootstrap uncertainty analysis described in the Methods section for each of the data sets analyzed in this work. ***d,*** Histograms of the thermal inertia solutions from the Monte Carlo bootstrap analysis.

Thermal model deviates slightly from the OVIRS data at some rotational phases. Near 0.4 rotational phase, for example, the largest boulder rotates into view on the limb of Bennu. This boulder has a fairly flat face and therefore receives direct sunlight and heats up quickly

when it rotates into sunlight. Based on its size measured in images, we estimate that the thermal radiance from this large boulder is consistent with the level of departure of the model from the data. However, the boulder, particularly its flat face, is not well represented in the global shape model. We therefore conclude that the deviations between the OVIRS data and thermal model are mostly due to remaining imperfections (such as poorly represented boulders) in the shape model. Nevertheless, ascribing those deviations to thermal inertia variations provides an upper limit to the amount of thermal inertia variation with rotation. Allowing thermal inertia to vary with rotation to ensure a perfect fit to the 4-µm lightcurve suggests variations of < 10 J m^{-2} K^{-1} s$^{-1/2}$ over a full rotational phase.

Global boulder counts
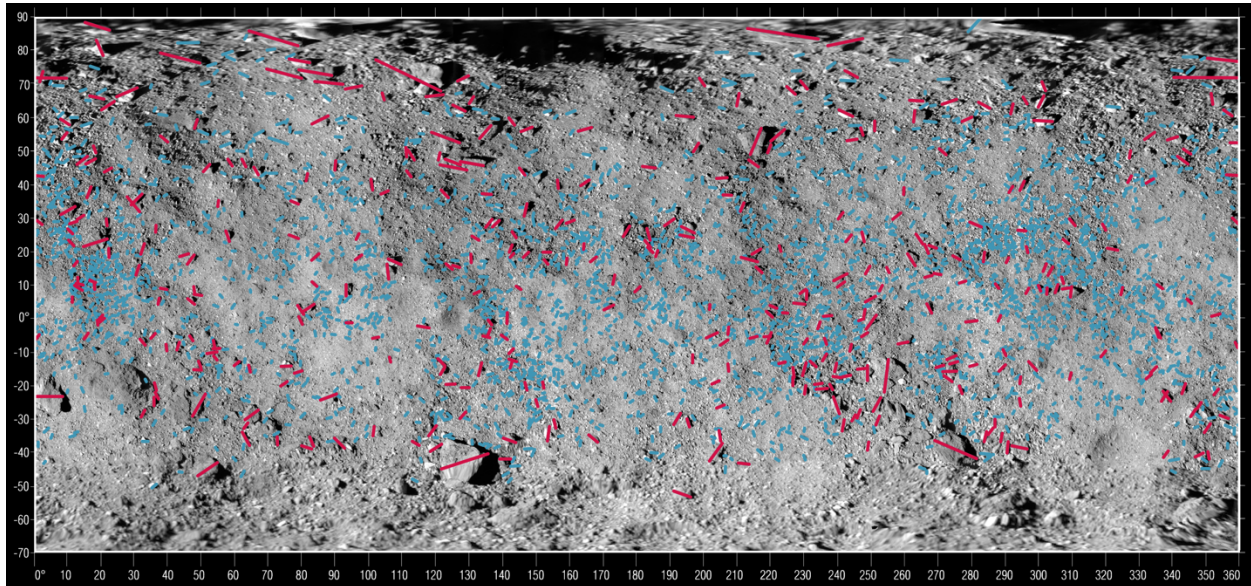
Supplementary Figure 3. The global mosaic of Bennu with an overlay of the shapefile generated from the boulder counts that cover ~80% of the surface of Bennu. These data were used in the cumulative size-frequency distributions presented in this work. Pink lines correspond to the counts that are greater or equal to the completeness limit of (~8 meters) and the blue lines indicate the counts that are below the completeness limit. The geometric information for the counts was calculated using shape model v13, using unprojected L2 OCAMS images (see methods). Counts were performed on unprojected PolyCam image taken on 1 December 2018 with pixel scales between 0.743 and 3.866 m/pixel. There are few to no counts close to the South Pole because the imaging campaign on 1 December did not provide adequate coverage of that area. This global mosaic is created by combining images from 1 December with MapCam images from 16 December 2018 with pixel scales from 0.831 to 1.625 m/pixel.

**Cumulative size-frequency distribution of Bennu and other small bodies**
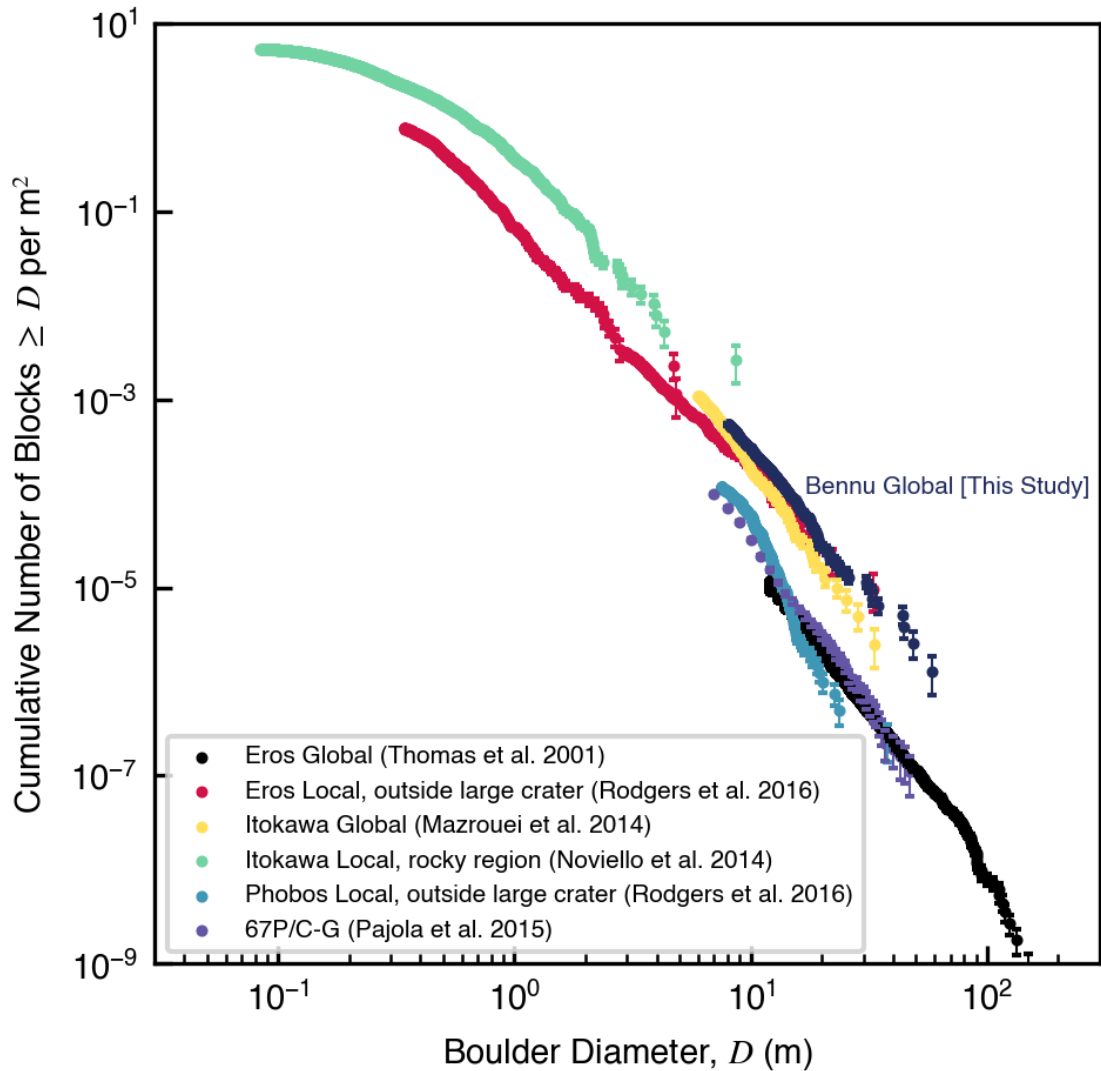
Supplementary Figure 4. The global unbinned cumulative size-frequency distribution (CSFD) of boulders on Bennu compared to several small Solar System bodies [30]. This shows that Bennu's CSFD is within the range observed on other small bodies.

Crater mass ejecta vs. size compared to Bennu's largest boulder and crater
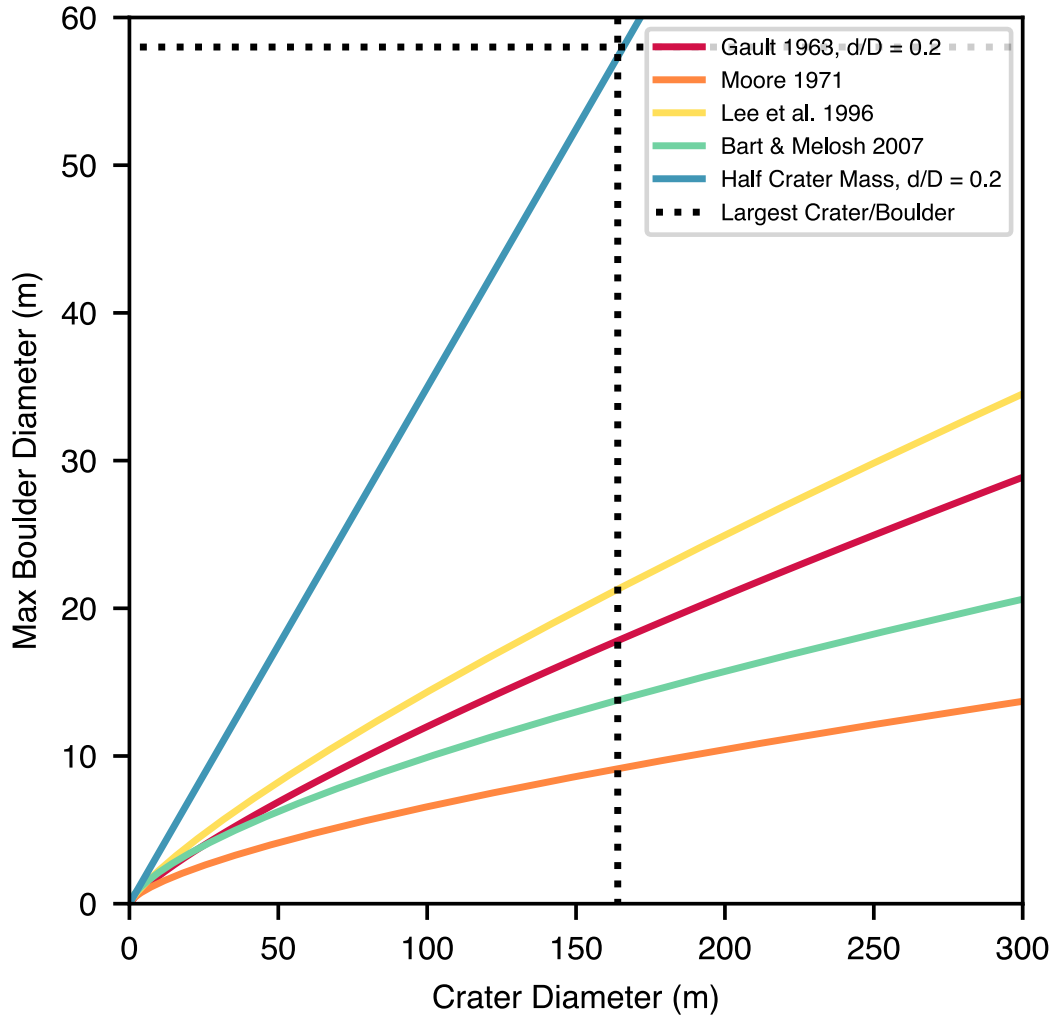

Supplementary Figure 5. The relationship between the mass distribution of crater ejecta and crater size according to several classic scaling law models (shown below). These models encompass analysis of the boulder size-frequency distribution related to impact craters on Earth [67], the Moon [68, 69], and the asteroid (243) Ida [24]. While boulder production through impacts on a rubble-pile asteroid may differ from these larger bodies, it is yet unclear how it scales across gravity and composition; nevertheless, we expect that the fundamental nature of boulder production through impacts to be similar. As a demonstration of the fundamental change in our understanding required to explain crater-related production of the largest boulders on Bennu, we show an unphysical scaling relationship that results in 50% of the crater ejecta being expelled as a single block is necessary to link the existence of the largest boulder (58 ± 6 m) to the largest crater (164 m) on Bennu. We assume conservative d/D of 0.2, compared to the 0.13±0.04 value reported by [3]. Therefore, based on our current understanding of boulder production through impact cratering, we conclude that the largest boulders on Bennu (> 20 m) are likely primordial.

08:00 LST

09:30 LST

11:00 LST

12:30 LST

14:00 LST
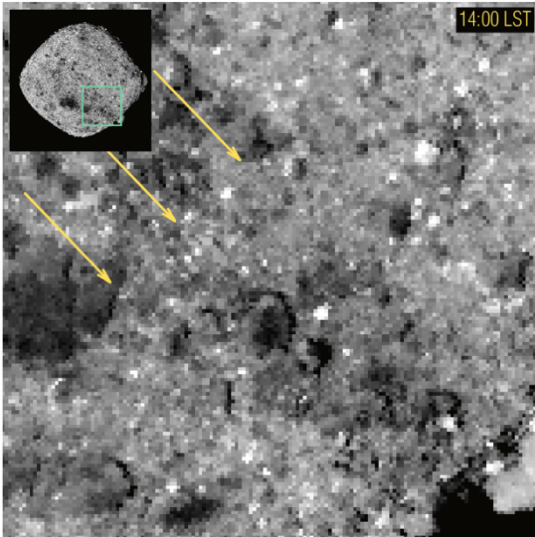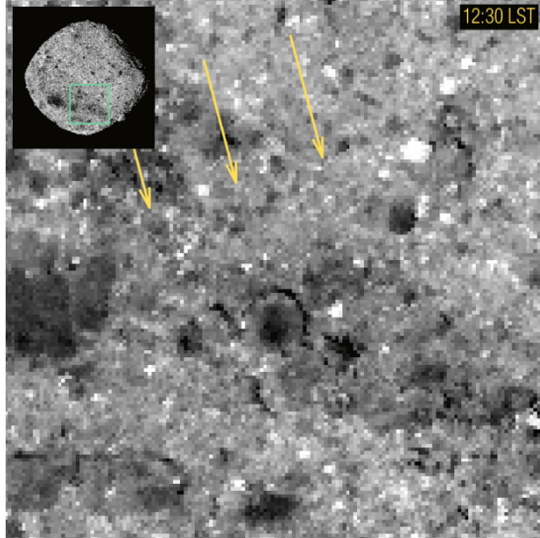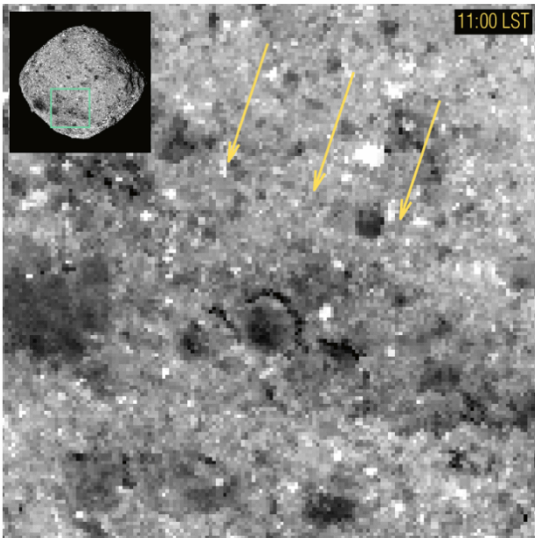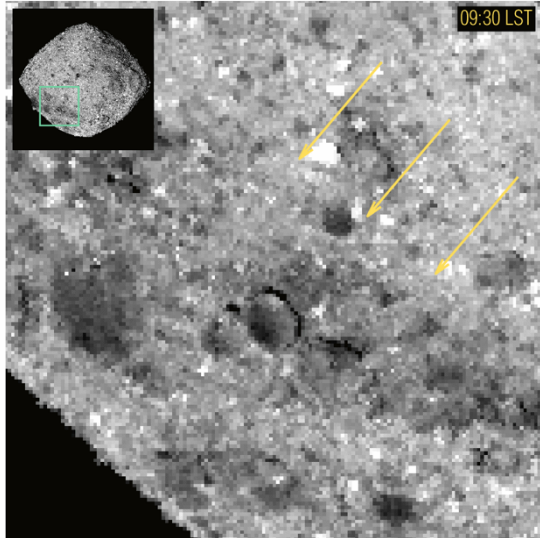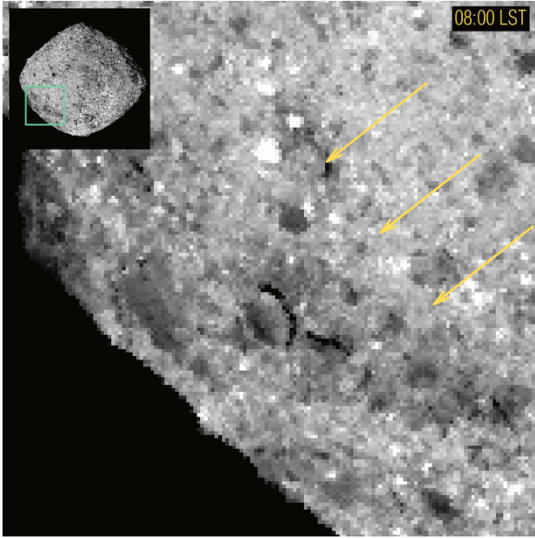
Supplementary Figure 6. A series of images taken on 25 November 2018, at a phase angle of ~4°, which highlights the same region shown in Figure 5 of the main text. Yellow arrows indicate the direction of sunlight; the time in the upper right corner is the Local Solar Time at the central boulder in the image; the inset indicates the region of interest on Bennu. All images have been stretched identically. Images show a consistent unit of dark diffuse material mantling the central boulder area. The consistent appearance of the dark material throughout a Bennu day indicates that these units represent albedo differences and are not shadowing due to terrain.

Surface roughness
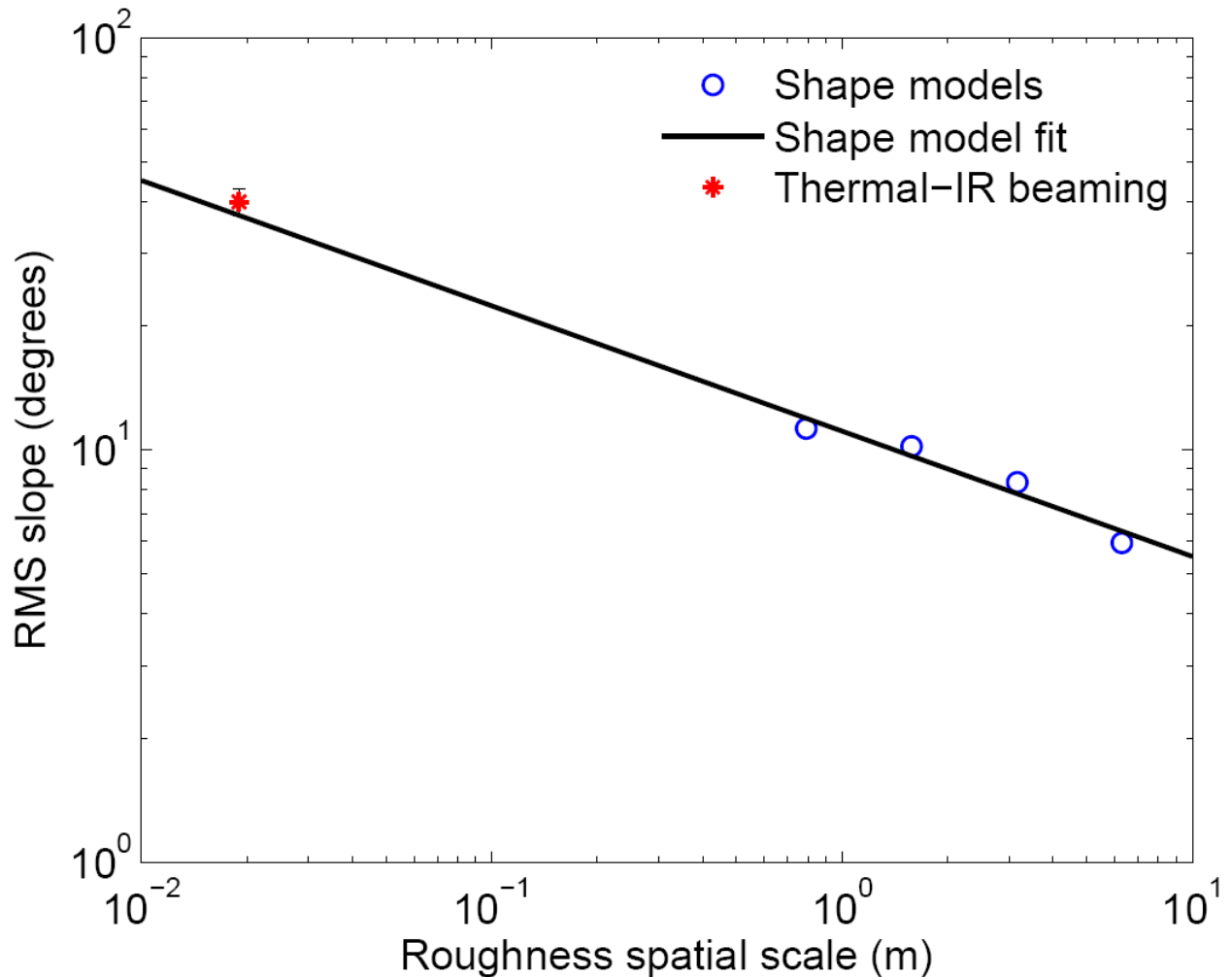
Supplementary Figure 7. Comparison of the roughness required to fit the observed thermal-infrared beaming from Bennu to roughness computed at the scales of different versions of the OSIRIS-REx shape model. Blue circles are roughness computed at scales of 6.3 m, 3.2 m, 1.6 m, and 0.8 m relative to the 12.6 m resolution shape model used for thermal analysis. The black line is a power-law fit to the blue circles. The red asterisk is the roughness determined from fitting the thermal data. It is placed at the roughness scale where the error bar crosses the extrapolation of the fit to the shape model roughness – about 2 cm. These results suggest that the thermal infrared beaming is most sensitive to the smaller end of the spatial scale (i.e., close to the thermal skin depth), and that Bennu is much rougher at these scales than at larger spatial scales. See [43] for more discussion of thermal infrared roughness.
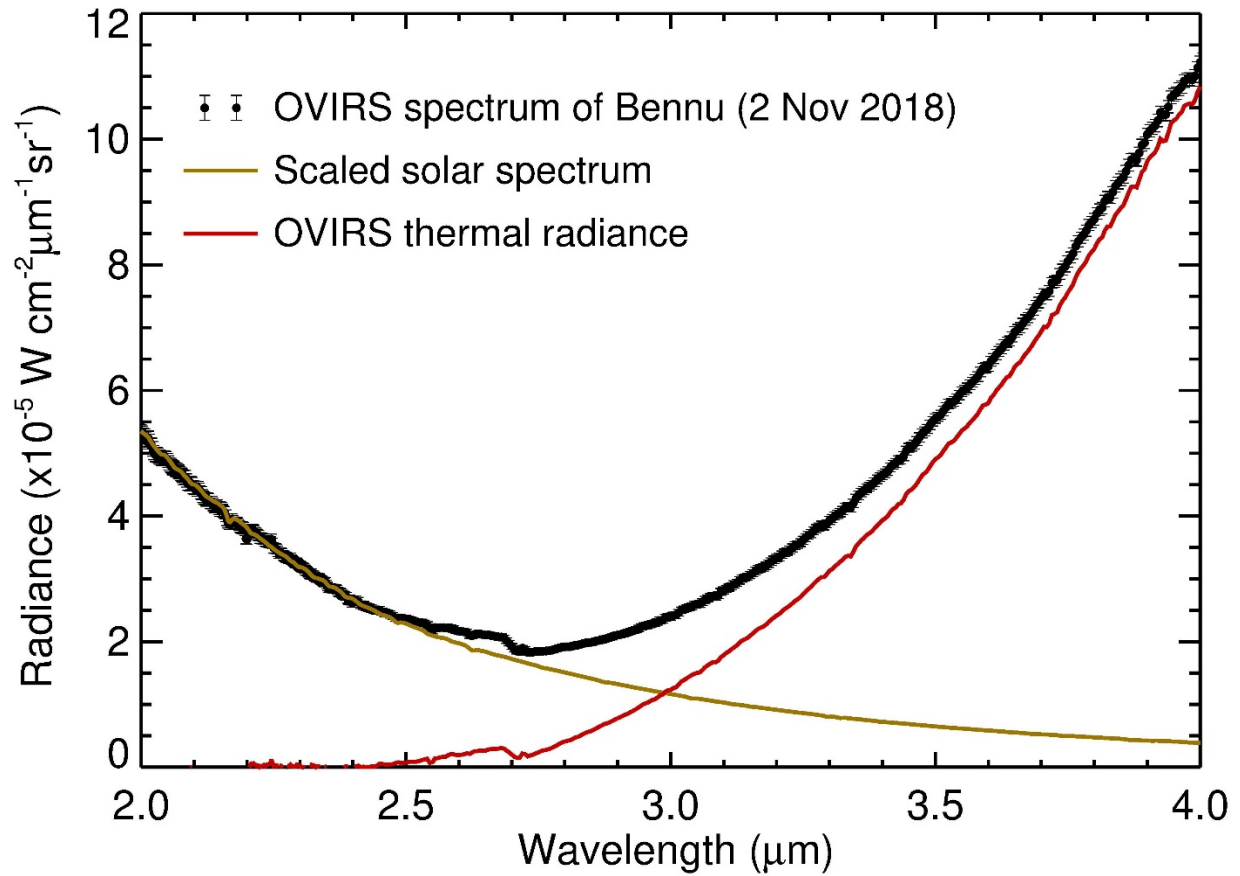
Supplementary Figure 8. Illustration of the isolation of thermal radiance in OVIRS data. The solar spectrum (gold line) was scaled to the observed OVIRS radiance (black points) at ~2.1 μm, where the data are dominated by reflected sunlight. The scaled solar spectrum represents the continuum reflected radiance from Bennu, assuming a flat spectral slope. This estimate of reflected radiance is then subtracted from the observed total radiance. The result is the thermal radiance (red line), which is used in the thermal analysis.